
CMS Physics Analysis Summary

Contact: cms-pog-conveners-lum@cern.ch

2019/05/24

CMS luminosity measurement for the 2018 data-taking period at $\sqrt{s} = 13$ TeV

The CMS Collaboration

Abstract

The calibration of the luminosity measurement by the CMS experiment in the 2018 proton-proton data taking at $\sqrt{s} = 13$ TeV is described. The principal calibration is derived from the analysis of the van der Meer scan program in CMS taken during LHC fill 6868. In addition, the performance and stability of the CMS luminometers are also evaluated using emittance scans taken throughout the course of the year. The systematic uncertainty in the absolute calibration from the van der Meer scan is derived with a precision of 2.1%, with the dominant contribution to the uncertainty arising from the x - y nonfactorization of the beam shape. The total systematic uncertainty, including terms from stability and linearity effects, is 2.5%.

1 Introduction

Precision measurement of the luminosity delivered to the CMS experiment [1] by the LHC is important for a variety of reasons. Online, the luminosity measurement provides realtime feedback on the LHC performance and operation, as well as to CMS operations such as measurements of trigger rates. Offline, the luminosity measurement is a crucial component of nearly every physics analysis, either for measuring the cross section of observed processes or for setting upper limits in searches for processes beyond the standard model.

A total of seven systems are used for measuring luminosity at CMS. The Pixel Luminosity Telescope (PLT) [2] and Fast Beam Conditions Monitor (BCM1F) [3] are dedicated systems for luminosity measurement, while the hadronic forward calorimeter (HF) uses a dedicated readout on an existing system. These three use a separate data acquisition (DAQ) system, called BRILDAQ, which operates independently of the main CMS readout, so that luminosity measurements can be provided regardless of the current operating state of the rest of CMS. In addition, three other methods, the drift tube luminosity (DT), the pixel cluster counting method (PCC), and the vertex counting method (VTX) use data from existing parts of the CMS detector to perform a luminosity measurement using the main CMS DAQ system. The PCC measurement uses the data collected with the standard CMS trigger system [4] with triggers requiring colliding bunches but not any specific event activity (“zero-bias”). Finally, the RAMSES detectors are part of the LHC environmental protection and monitoring systems, but also can be used to provide a luminosity measurement read out through Timber, the operational data and LHC logging service.

Each luminometer reads out a rate of the specific quantities observed in the detector (hits, tracks, clusters, etc.). This rate, R , should be proportional to the instantaneous luminosity, $\mathcal{L}_{\text{inst}}$, with the constant of proportionality given by the visible cross section σ_{vis} :

$$R = \mathcal{L}_{\text{inst}}\sigma_{\text{vis}}. \quad (1)$$

In practice, the luminometers usually exhibit some nonlinear dependence on the instantaneous luminosity, the pileup (average number of interactions per LHC bunch crossing), or on external factors such as the LHC filling scheme; these nonlinearities need to be corrected to obtain an accurate measurement.

The determination of σ_{vis} is carried out through van der Meer (VdM) scans performed with a dedicated LHC machine setup. In these scans, the two beams are separated and then moved across each other, and the resulting measurement of rate as a function of beam separation can be used to derive the beam overlap width. The absolute luminosity value can subsequently be derived as a function of machine parameters [5] and the measured rate can be used to derive σ_{vis} . Then, this measurement can be used to determine the luminosity in regular physics fills, during which the beam overlap width cannot be measured with the necessary accuracy. This scan method has previously been used by the LHC experiments for the absolute luminosity scale calibration under various LHC running conditions [6–12]. This analysis describes the calibration of the luminosity measurement for proton-proton (pp) collisions at $\sqrt{s} = 13$ TeV during the 2018 LHC run.

2 Luminometers at CMS

2.1 The PLT detector

The PLT is a dedicated system for measuring luminosity using silicon pixel sensors, installed at the beginning of 2015 for Run 2. There are a total of 48 sensors arranged into 16 “telescopes”, eight at either end of CMS outside the pixel endcap, where each telescope contains three sensor planes arranged nearly parallel to the beam pipe. The sensors measure $8 \times 8 \text{ mm}^2$, divided into 80 rows and 52 columns, although, to reduce the contribution from background, only the central region of the sensors is used. The readout is performed using the PSI46v2 readout chip. The PLT measures the rate of “triple coincidences”, where a hit is observed in all three planes, typically corresponding to a track from a particle originating at the interaction point. The overall mean rate for PLT (and also in BCM1F) is estimated using the zero-counting method, where it is assumed that the number of observed triple coincidences follows a Poisson distribution with a mean μ , which is measured using the fraction of events f_0 where no triple coincidences are observed: $\mu = -\ln f_0$.

Over the course of 2018, accumulated radiation damage in the sensors resulted in a significant loss of efficiency in the PLT. The effects of this damage were compensated by increasing the high voltage applied to the sensors and adjusting the thresholds to record a hit; however, there were still several periods where the PLT had lower efficiency. Corrections for these efficiency losses are applied offline.

2.2 The BCM1F detector

The BCM1F measures both luminosity and machine-induced background (MIB). It consists of a total of 24 sensors mounted on the same carriage as the PLT. At the beginning of 2017, the sensors in the BCM1F were replaced and consist of a total of 10 silicon sensors, 10 polycrystalline diamond (pCVD) sensors, and 4 single-crystal diamond (sCVD) sensors. The pCVD and sCVD sensors use split-pad metallization, with each sensor having two readout channels, to keep the overall occupancy low given the expected conditions in Run 2. The BCM1F readout features a fast readout with 6.25 ns time resolution; the precise time measurement, in conjunction with the position of BCM1F 1.8 m from the center of CMS, allows hits from collision products to be separated from hits from MIB, because the incoming background is separated in time from the outgoing collision products. In the 2018 luminosity calibration presented below, only the pCVD sensors are used.

The BCM1F luminosity measurement is affected by “afterglow”, where a colliding bunch produces an exponentially decaying signal for several bunches afterwards due to activation of the surrounding detector material. This effect is measured by using data from empty bunches, which should nominally have zero luminosity, and corrections are derived and applied to the raw luminosity.

2.3 The HF measurement

The HF luminosity measurement, which has provided the primary online luminosity measurement for CMS, uses a dedicated readout system installed in the HF calorimeter; while this readout is available for the whole of HF, only two HF rings are used for luminosity measurement, to ensure relatively uniform occupancy. Two algorithms are available. The original one relies on the fraction of occupied towers (HFOC), while a new method implemented in 2016 is based on the sum of the transverse energy E_T (HFET). In 2018, the primary algorithm is chosen to be HFOC.

Both algorithms require two types of corrections to account for afterglow effects. “Type 1” corrections account for the signal from a hit spilling over into the next 25 ns bunch crossing (BX) after a colliding bunch, while “type 2” effects account for an exponentially decaying afterglow, as for BCM1F. As in the BCM1F case, these effects are measured and corrections derived using data from empty bunches. The afterglow corrections (combining type 1 and type 2) for HFOC (HFET) amount to approximately 0.9% (4%) in the bunch immediately following a colliding bunch and 0.2% (0.5%) in the next following bunch, with the corrections for subsequent bunches less than 0.2% (0.1%).

For HFOC, there is an additional type 1 effect, the “bunch train effect”. The HFOC algorithm includes an analog-to-digital converter (ADC) threshold. It is hypothesized that with a signal from the previous bunch still at an appreciable level, yet under the ADC threshold, an additional signal in the current window can exceed the effectively reduced threshold; that is, the sum of the two weak signals will be over the ADC threshold even though the individual signals could be well below it. The previously described method for estimating type 1 afterglow does not account for this contribution that lies on top of all per bunch luminosity except for the first bunch among a group of consecutive bunches (i.e., a bunch train). A dedicated study is performed comparing the double ratio of the HFOC measurement for the first bunch over the measurement averaged over the next four bunches divided by the same ratio of HFET; this ratio is fitted with a function of the form $1 + p_0x + p_1x^2$ and used to obtain a luminosity-dependent correction. This correction is modeled with a first-order polynomial as a function of the single-bunch instantaneous luminosity (SBIL) and amounts to about 0.5 and 2% at SBIL = 2 and 10 Hz/ μ b, respectively.

Over the course of 2018, aging effects in the photomultiplier tubes and optical fibers in HF result in a small but measurable loss of efficiency for both the HFOC and HFET methods. This efficiency loss is measured and corrections are applied offline, as described in Section 6.

Finally, contributions from noise can be significant at low-pileup conditions. The noise in the detector is estimated by taking the average rate of the first 50 non-active bunch crossings, after the afterglow correction has been applied. This value is then subtracted from the HFOC measurement for all bunch crossings.

2.4 The PCC method

The PCC method uses the rate of pixel clusters in the CMS pixel detector to provide a luminosity measurement. It supplied the primary offline luminosity measurement for CMS in 2015–2016, since the large area of the pixel detector and the relatively low occupancy provides a measurement with good statistical precision, and the stability of the measurement over time is typically good. Because the CMS trigger bandwidth available for collecting the data used for this measurement is limited, the statistical precision for a single 23-second period (“luminosity section”) is not as high as for the online luminometers, but integrated over longer time periods it provides stable, high precision luminosity measurement. For the VdM measurement, a special trigger mode is used which provides a higher data rate for PCC, so it can acquire enough data to attain the necessary statistical precision, but these data are taken only for five bunch crossings.

In the PCC measurement, the innermost layer of the pixel detector is excluded because it is significantly affected by dynamic inefficiency effects, where the hit efficiency decreases at higher $\mathcal{L}_{\text{inst}}$ due to the readout chip not being able to process all of the hits. Only modules that are found to operate consistently well for luminosity purposes during the year are used in the measurement. In total, approximately 40% of pixel modules are used for the final measurement.

As for the HF luminosity, type 1 and 2 corrections are measured and applied to the PCC measurement. Since these corrections varied over the course of the 2018 run, they are measured as a function of time and applied in a time-dependent manner. The afterglow corrections for PCC are in the range 2–3% for the type 1 corrections and 6–7% for the total correction, averaged over all active bunches. A correction for detector noise is also applied.

2.5 Vertex counting

Counting reconstructed pp collisions is a reliable method for low pileup luminosity estimates. Primary interaction vertices can be reconstructed using tracks that point back to a well-defined point in space (with a precision of about 10 microns [13]). At high pileup, vertices often occur very close together and so they are indistinguishable with track reconstruction algorithms alone. However, in fills for calibration analyses, the pileup is so low that there are usually only 0 or 1 pp collisions in a single crossing, and so the nonlinearity due to vertex merging is expected to be insignificant.

Although the vertex reconstruction is not completely efficient [13], the background to this measurement is negligible. Consequently, vertex counting provides excellent profiles of beam shape overlaps. The main drawback of this luminometer is that not enough data can be acquired in order to achieve good statistical precision for each bunch crossing. As the vertex counting uses the same zero bias data sample that is collected for PCC, only five bunch crossings in a VdM fill are typically considered by the DAQ.

While not explicitly required for vertex counting, vertex quality cuts are often desirable for other studies using vertices and are applied for vertex counting as well. The most important selection is to typically ask for a large number of tracks (14 in this analysis) to be associated with the vertex in question. The efficacy of the vertex counting method is unaffected by this selection.

2.6 The DT measurement

The DT luminosity measurement uses the rate of muon track stubs in the muon barrel track finder. While the DT measurement is available to the BRILDAQ and is thus available online, the DT algorithm used does not provide bunch-by-bunch measurements and is thus applicable only for the total luminosity measurement. In Run 2 the DT measurement has generally been stable and linear, as long as the track finder itself is not changed, so it provides a complementary offline reference measurement. The rate in DT during VdM fills is too low to allow for calibration using the VdM scan, so it is cross-calibrated to another detector.

2.7 The RAMSES detector

RAMSES is a CERN radiation and environmental monitoring system, currently a part of the REMUS supervisory system. It was introduced in the beginning of the LHC era with originally 8 monitors installed in the CMS experimental cavern. Then two additional detectors were installed during Run 2.

The sensor itself is a cylindrical plastic ionization chamber filled with 3 L of air at atmospheric pressure; the walls are coated with 4 mm of PE graphite. It primarily detects photons within the energy range of 50 keV to 7 MeV (reference calibration at 662 keV). Current collected on the anode is translated into the ambient dose equivalent rate providing measurements in the range 5 μ Sv/h to 500 mSv/h (corresponding to a current in the range 1.4×10^{-13} – 1.4×10^{-8} A). The broad measurement range allows real-time monitoring in the working environment during

LHC operation as well as stops and shutdowns. The data is published via DIP and Timber, facilitating further data analysis.

Although RAMSES is not designed as a luminometer, the rate observed in the RAMSES detectors does function quite well as a luminosity measurement. The overall rate in the RAMSES detectors is small, which means that it is not capable of making bunch-by-bunch measurements and cannot be independently calibrated using a VdM scan; however, this also means it is less affected by issues such as instability caused by radiation damage or nonlinearity caused by high rates over the course of the 2018 run.

3 Van der Meer scans

3.1 Calibration with VdM scans

The instantaneous luminosity for a single colliding bunch i , $\mathcal{L}_{\text{inst}}^i$, can be expressed as a function of beam parameters. If there is no crossing angle between the beams and the beams collide with zero relative separation (“head-on”), the instantaneous luminosity is given by the formula:

$$\mathcal{L}_{\text{inst}}^i = N_1^i N_2^i f \int \rho_1(x, y) \rho_2(x, y) dx dy = N_1^i N_2^i f \int \rho_{x1}(x) \rho_{x2}(x) dx \int \rho_{y1}(y) \rho_{y2}(y) dy, \quad (2)$$

where N_1^i and N_2^i are the number of protons in the two individual beams for the colliding bunch i , $f = 11\,246$ Hz is the LHC orbit frequency, and ρ_j is the normalized particle density for the bunch in beam j . The rightmost term of Eq. (2) uses the assumption that ρ can be factorized into independent terms in x and y , $\rho_x(x)$ and $\rho_y(y)$, respectively.

The measurement of the beam currents N^i is well determined, but the individual proton density functions cannot be directly measured. The VdM method determines the value of the two beam overlap integrals in Eq. (2) by varying the beam separation and measuring the resulting rates:

$$\int \rho_{x1}(x) \rho_{x2}(x) dx = \frac{R_x(0)}{\int R_x(\Delta) d\Delta}, \quad (3)$$

where $R_x(\Delta)$ is the rate measured when the two beams are separated in x by a distance Δ ; a similar equation can be written in y . We then define the beam overlap width Σ_x (and similarly Σ_y) as:

$$\Sigma_x = \frac{1}{\sqrt{2\pi}} \frac{\int R_x(\Delta) d\Delta}{R_x(0)}, \quad (4)$$

yielding the final expression for luminosity:

$$\mathcal{L}_{\text{inst}}^i = \frac{N_1^i N_2^i f}{2\pi \Sigma_x \Sigma_y}. \quad (5)$$

In practice, the integral in Eq. (4) is evaluated by performing two separate scans in the x and y directions, measuring the rate (normalized by the product of the beam currents) at a certain number of separation steps, fitting the resulting points with a functional form, and using the fitted function to determine the overall integral. This procedure is described in more detail in Ref. [14]. Once Σ_x and Σ_y are determined, then Eq. (1) can be used to obtain the overall visible

cross section σ_{vis} . Since Eq. (1) should hold for all beam conditions, the σ_{vis} thus obtained can be used to determine the luminosity in regular beam conditions, not just the special VdM conditions. This is because the detector acceptance should not change between the two conditions; this has been verified previously in a special fill where the crossing angle was changed in steps from 150 to 120 μrad , and no change in measured σ_{vis} within uncertainties was observed.

Before performing the fit to extract Σ_x and Σ_y , the raw measured rates must be corrected for background in the detector. The background contribution is estimated independently, using two special periods, each 5 minutes long, during the VdM scan where the beams were separated by $6\sigma_b$ (where σ_b is the beam size) in both the x and y directions, ensuring that the only contribution is from background (either beam-induced background or detector noise). The estimated background is then subtracted from the raw data before the fit is performed using a single Gaussian function, which was found in 2018 to adequately describe the measured rates as a function of beam separation. This procedure is used for PCC, PLT, BCM1F, and HFOC, but not for HFET and vertex counting, since the constant terms for these are negligibly small (less than 0.1%). The measured background is 0.4% for PCC, 0.3% for PLT, 0.5% for BCM1F, and 0.8% for HFOC relative to the rates measured at head-on collisions (that is, with $\Delta = 0$). The uncertainties in these measurements are about 5, 30, 20 and 10%, respectively, relative to the measured background, and they are propagated to the fit where the σ_{vis} is extracted. A systematic uncertainty of 0.1% is assigned to the final calibration result to account for the uncertainty in the background subtraction.

As described in detail in Section 4, several other corrections are applied to the raw data before the VdM fit is performed. These corrections take into account drifts in the position of the LHC orbit, beam-beam interaction effects, and the beam separation length scale. The event rates are normalized by the bunch intensities before the fit. The intensities are measured by the LHC beam current monitors and are corrected for bunched spurious (so-called “ghost” and “satellite”) charges.

Figure 1 shows an example of the VdM fit procedure for PCC for an individual bunch with bunch crossing ID number (BCID) 865.

3.2 2018 scan program

The VdM scans were performed during LHC fill 6868 on June 30 and July 1, 2018 at $\sqrt{s} = 13\text{ TeV}$. The LHC filling scheme was `525ns_140b_124_32_23_16bpi_11inj` with 124 colliding bunch pairs at the CMS interaction point (IP5) widely spread over the orbit to reduce long-range beam-beam effects and detector afterglow. Special LHC beam optics were used for the fill, with $\beta^* = 19.17\text{ m}$ and transverse emittances of $\epsilon_{h,v} \approx 1.5\text{--}3.5\ \mu\text{m}$. For 2018, the emittance of the bunches was selected in two different ranges, to allow for studies of bunches with different beam size. The resulting beam size σ_b at the beginning of the fill was in the range of approximately 85–95 and 80–90 μm in x and y , respectively, increasing over time in the x dimension and decreasing over time in the y dimension. No crossing angle was used for collisions at ATLAS and CMS. The resulting peak pileup was approximately $\mu = 0.6$, much lower than in a regular physics fill.

The bunch intensities were approximately $7\text{--}9 \times 10^{10}$ protons per filled bunch, resulting in a total beam intensity of slightly above 10^{13} protons per beam. The total beam intensities were measured with the DC Current Transformers (DCCT) [15], and the bunch currents were measured with the Fast Beam Current Transformers (FBCT) [16]. The beam orbit was monitored using two systems, the DOROS beam position monitors (BPMs) [17] located near IP5, and the arc BPMs located in the LHC arcs adjacent to CMS. The orbit is also tracked using movements

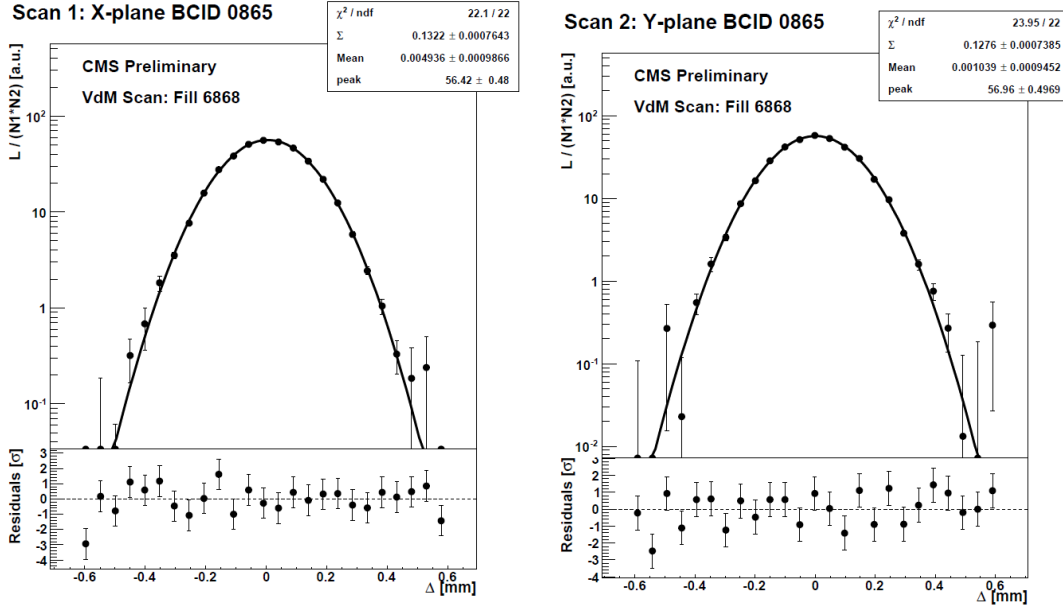


Figure 1: Normalized rates and the resulting fitted single Gaussian scan curves as a function of the beam separation (Δ) for a single bunch (BCID 865) as recorded by PCC for a scan in the x (left) and y direction (right). Background subtraction and the corrections described in the text have been applied to the raw data before the fit.

of the luminous region based on reconstructed vertices. The arc BPM measurements are translated to a beam position at IP5 using the LHC optics file; the specific optics file used for this scan is R2016c_A19mC19mA19mL24m.

To ensure a dataset with a high event count for PCC even at large beam separations, CMS gated the zero-bias triggers on 5 bunch pairs (BCIDs 265, 865, 1780, 2192, and 3380) and recorded events with a total rate of 27.7 kHz.

The CMS VdM scan program was conducted in two parts (“takes”), due to an alarm. The first part consisted of a total of six x - y scan pairs. Two (“emit1” and “emit2”) were short “emittance” scans, in which the two beams were separated by $4\sigma_b$ in 9 steps with 10 seconds integration time at each scan point. Scan pair “norm1” was a standard VdM scan, in which the two beams were separated by $6\sigma_b \approx 600 \mu\text{m}$ and scanned across one another in a sequence of 25 steps with 30 seconds per step. Then “offset1” was an “offset” scan, with the same procedure as the standard scans except that the beams were separated by $\pm 1.5\sigma_b$ in the nonscanning direction. Finally, two pairs of “beam imaging” scans were conducted, in which one beam (beam 1 in the first pair, followed by beam 2 in the second pair) is kept fixed at its nominal position while the other is separated and scanned in 19 steps from $+4.5\sigma_b$ to $-4.5\sigma_b$ with 46 seconds per step. The second scan pair was interrupted by an alarm followed by a power cut just before its completion, so only “imag1” can be used for analysis.

The second part of the scan program was conducted in the same fill but about 7.5 hours later. It consisted of twelve scan pairs. Scan pair “emit3” was a short emittance scan, followed by scan pairs “imag2” and “imag3” of the beam imaging kind, an offset scan pair “offset2”, and finally two normal VdM scan pairs “norm2” and “norm3”. The latter two allow us to test the reproducibility of the measurement.

A length scale calibration (LSC) was performed after scan pair “norm3” using two different

methods. The first, “lsc1”, was the “constant separation” scan, in which the two beams were separated by $1.4\sigma_b$ (approximately equal to 1Σ) and moved together in steps of $1\sigma_b$ across and back, for a total of 10 steps with 70 seconds per step, once in each transverse direction. A second “variable separation” method with scan pair “lsc2” was also executed, in which one beam (starting with beam 1) is moved to $-2.5\sigma_b$ and then a three-point scan (a “miniscan”) is performed with the other beam (starting with beam 2) at a relative position of $-1.25\sigma_b, 0$, and $+1.25\sigma_b$. The position of the first beam is then translated in five steps in the same direction to $+2.5\sigma_b$, repeating the miniscan at each step. This procedure is repeated four times, with two directions for each of the two beams. Each scan point has a duration of about 46 s.

Finally, a normal VdM scan pair “norm4” and two short emittance scan pairs “emit4” and “emit5” concluded the program.

In each scan pair, the scan was performed first in the x direction and then in the y direction, with the exception of the variable separation length scale calibration scan pairs, which were done the other way around.

Figure 2 shows the beam positions for the two beams in the x and y directions as measured by the DOROS BPMs during the scan program, showing all 18 scan pairs.

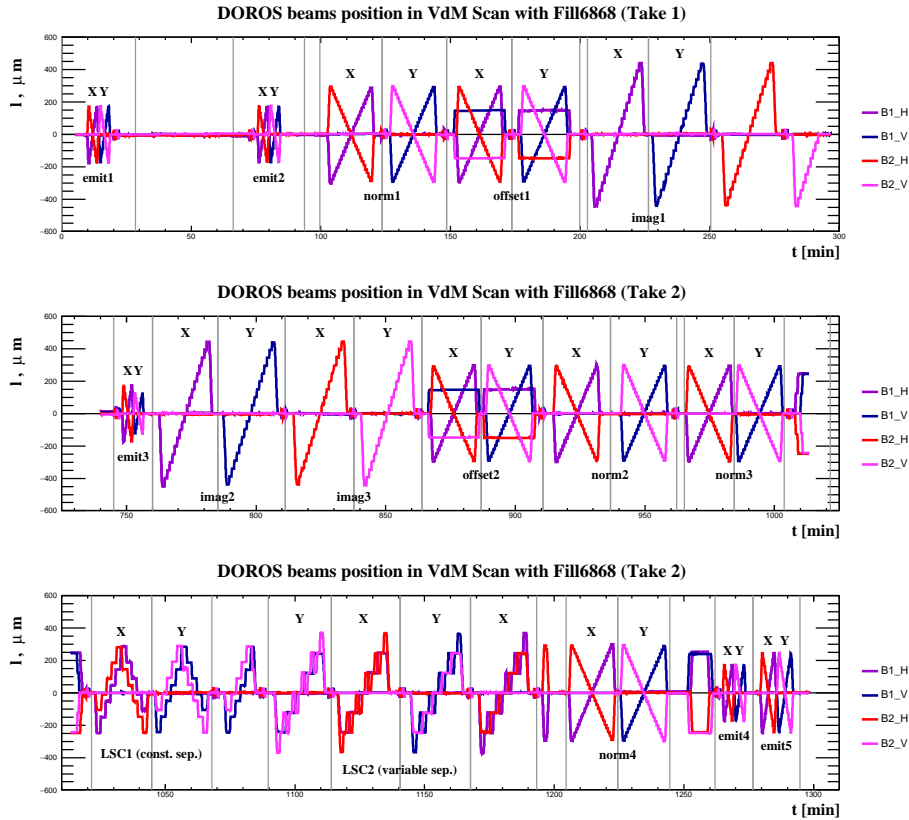


Figure 2: Relative change in beam positions measured by the DOROS BPMs during the 2018 scan program for the two individual beams in the horizontal x and vertical y planes, as a function of the elapsed time from the beginning of the program. The top row shows the portion of the scan program before the alarm at CMS, while the bottom two rows show the scan program after the alarm.

The beam imaging and offset scans are intended for specific studies on the beam shapes described in Section 4, and they can also be analyzed as traditional van der Meer scans. Both

the LSC and beam imaging scans are discussed in detail in Ref. [18]. The offset scan data is analyzed for the first time in 2018.

4 Corrections and systematic uncertainties

There are several systematic effects which affect the beam overlap width measurement, and hence the σ_{vis} extracted from the VdM scan procedure. These effects are measured and, where applicable, corrected as described below, and a systematic uncertainty is assigned to the resulting measured cross section for each source.

4.1 Length scale calibration

The length scale calibration is used to measure possible differences between the actual and nominal beam separations during the scans, exploiting the high precision of the CMS inner tracker. In order to measure this effect, a dedicated length scale calibration consisting of two separate scans, as described in Section 3.2, is conducted.

4.1.1 Constant separation scan

In the constant separation scan, the beams are separated and moved together first in the x direction and then in the y direction. The CMS tracker is used to reconstruct the position of the luminous region and the resulting position is plotted against the nominal separation; a linear fit is then applied to extract the resulting correction and its uncertainty.

Figure 3 shows the results of the scans in the x and y directions with the forward and backward parts of the scan shown separately; in this plot, the difference between the reconstructed luminous region position and nominal beam position is shown, so the resulting slope directly yields the necessary correction. In order to obtain the final length scale correction, the resulting slopes are averaged over the two parts, yielding a correction of -0.7% and -0.3% in the x and y direction, respectively, resulting in a total reduction in σ_{vis} of $0.9 \pm 0.1\%$, where the uncertainty derives from the statistical uncertainties in the fitted slope.

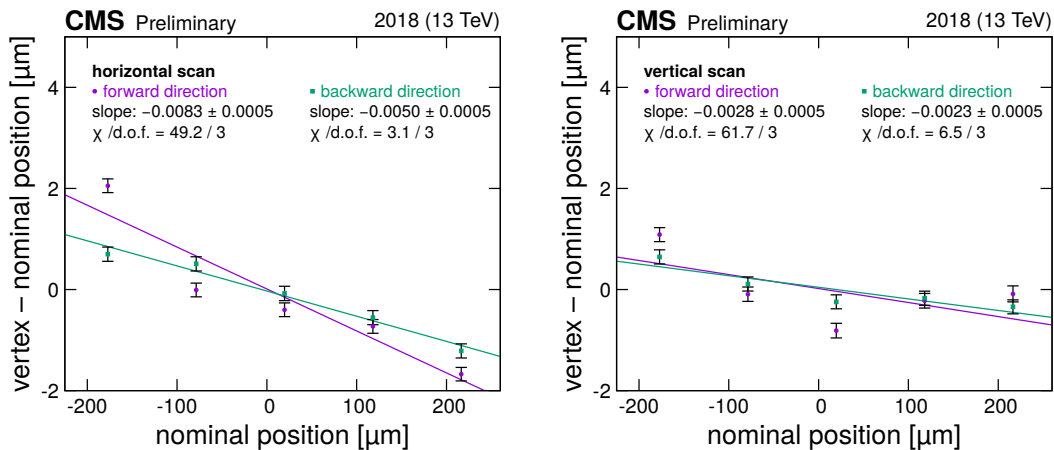


Figure 3: Difference between reconstructed luminous region position and nominal beam separation, as a function of the nominal beam separation, in the constant separation LSC scans. Left: scan in the x plane, for the forward (purple) and backward (green) scan directions. Right: same for the y plane. The plots are fitted with a straight line to derive the correction.

The systematic uncertainty in this correction is derived from four sources: the variation in the forward and backward parts of the scan (0.2%), the effect of orbit drift during the LSC scan

(0.2%), the effect of tracker misalignment (0.03%), and inconsistency in measuring the average vertex position between taking a fit or the simple mean (0.2%). The orbit drift measurement is discussed further in Section 4.2. Added in quadrature with the statistical uncertainty, the total uncertainty is 0.3%.

4.1.2 Variable separation scan

Like the constant separation scan, the variable separation scan uses the CMS tracker to reconstruct the displacement of the luminous region. As described in Section 3.2, one beam is scanned in five points and at each point the second beam performs a miniscan relative to the first beam. For each miniscan, the mean vertex position is determined using a fit with a Gaussian function and plotted against the nominal beam separation. Then, the vertex rate as a function of the nominal beam separation is fit with a second Gaussian to obtain the luminous region position at the point of maximum beam overlap. Finally, we plot the resulting five luminous region positions as a function of the nominal displacement of the first beam. Thus, the scan produces a measurement of the calibration constant in each direction for each beam separately. The calibration data for both horizontal and vertical bumps of beam 1 and beam 2 are presented in Fig. 4; as in the constant separation plots, the difference between the reconstructed luminous region position and nominal beam position is shown. Because normal VdM scans are performed by displacing the two beams symmetrically in opposite directions, the final correction value is given by the average of the corrections for beam 1 and beam 2 in each plane; i.e., $(-0.0027 - 0.0072)/2 \approx -0.49\%$ and $(-0.0004 - 0.0015)/2 \approx -0.10\%$ in the x and y directions, respectively; these results agree with those from the constant separation scan within uncertainties. Because of the large χ^2/ndof value of the fits, we scale the statistical uncertainties in the fit parameters by $\sqrt{\chi^2/\text{ndof}}$, resulting in an uncertainty of 0.1% in the x plane and 0.2% in the y plane, for a total statistical uncertainty of 0.3%.

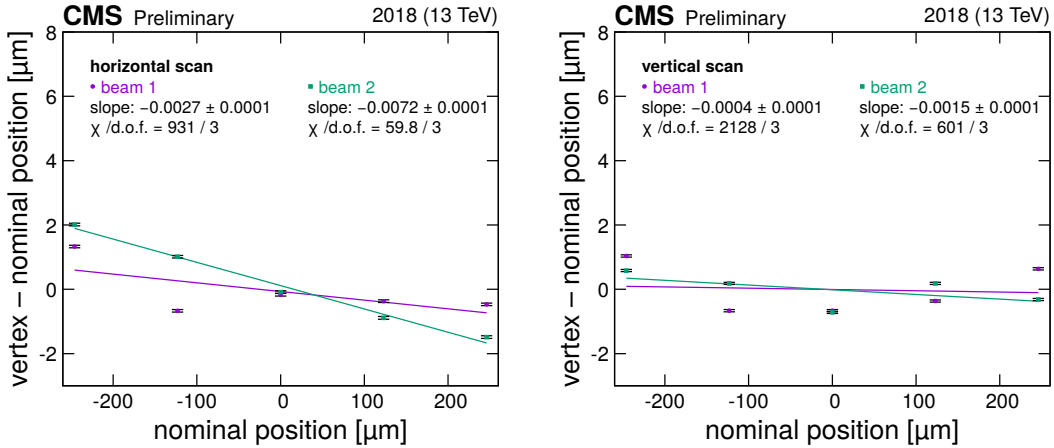


Figure 4: Length scale calibration scan, using the variable separation procedure, for the x (left) and y (right) direction of beam 1 (purple) and beam 2 (green), respectively. The difference between the reconstructed luminous region position and nominal beam separation, as a function of the nominal beam separation, is shown. The line is a linear fit to the data. Errors are of statistical nature.

The impact of orbit drifts during the variable separation scan is evaluated by comparing the length scale correction with and without orbit drift correction applied using the measurements of the arc BPMs. It is found to be 0.05% in the x and 0.01% in the y direction. The total final correction value is thus $(-0.6 \pm 0.3)\%$.

The final uncertainty in the length scale calibration is evaluated by combining the results from the two independent scan methods. We average the two scan results to get the final correction and its uncertainty of $(-0.8 \pm 0.2)\%$.

4.2 Orbit drift

The orbit drift correction accounts for potential movement of the LHC orbit during the VdM scans. The beam position is measured using two separate beam position monitor systems, the DOROS BPM system and the arc BPMs, with the former used as the primary measurement and the latter as a cross-check. The beam position measurements are taken before and after each scan, as well as at the scan point where the beams are head-on. For each scan, a linear interpolation on the beam position is made from the point before the scan to the head-on point and used to derive the correction for the first half of the scan, and similarly a linear interpolation from the head-on point to the point after the scan is used to correct the second half of the scan.

Figure 5 shows the measured positions along with the resulting fits for one portion of the VdM scan period (the first half after the interruption at CMS). In general, the orbit drift during the 2018 VdM scans is quite small, less than 10 and 5 μm in the x and y direction, respectively, for most of the scans. Nonetheless, the beam separation values are corrected for this effect, which changes the σ_{vis} by 0.2%. The systematic uncertainty of this correction is 0.01%, and it is evaluated by comparing the σ_{vis} values with orbit drift corrections taken from the DOROS and the arc BPM measurements.

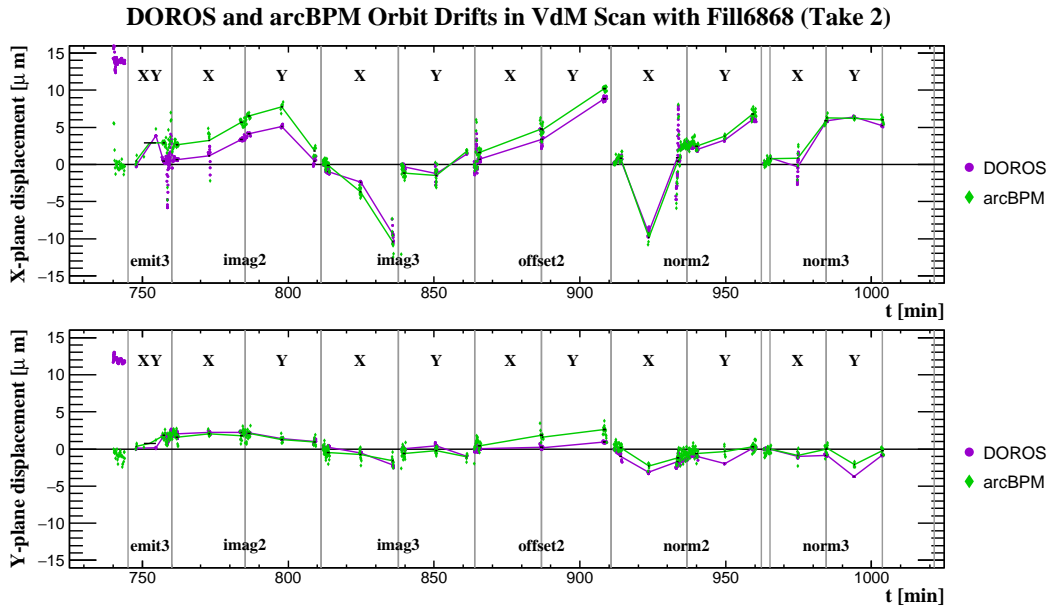


Figure 5: Results of the orbit drift measurement in x (top) and y (bottom), during the first half of the scan program after recovery from the fire alarm at CMS. The dots represent the beam position measured at the times when the beams are head-on before, during, and after each scan, as given by the DOROS BPM and arc BPMs in μm . The lines are the interpolations used to provide the orbit drift correction for each scan step.

Because the beams are not always exactly at the head-on position when their nominal separation is zero, taking the rate at the nominally head-on point may not give the true peak of the rate vs. separation curve, as discussed in Section 6. To account for this effect, a peak position correction is applied. The size of this correction decreases when the orbit drift correction is

applied, and its effect on the visible cross section is well below 0.1%. Because the peak position and orbit drift corrections are correlated, a common conservative 0.1% uncertainty is taken.

4.3 Effect of x - y nonfactorization

4.3.1 Beam imaging analysis

The VdM scan method assumes that the bunch proton density function is factorizable into independent x - and y -dependent terms. However, this assumption is not strictly valid, and can lead to a biased estimate of the beam overlap area. In order to measure this effect, special beam imaging scans, as described in Section 3.2, are conducted. In these scans, the measured vertex position distributions are used to derive the bunch proton densities, which can then be used to estimate a correction to the visible cross section. In particular, as the moving beam is scanned across the stationary beam, the resulting two-dimensional vertex distribution can be used to measure the bunch proton density of the stationary beam. The resulting distribution is then fitted with a function to reconstruct the overall distribution. The procedure for reconstructing bunch proton densities and deriving corrections in this manner is described in detail in Ref. [19].

The simplest model for the bunch proton density that has a correlated spatial dependence is a Gaussian distribution with x - y nonfactorization parametrized by a correlation parameter ϱ :

$$g(x, y) = \frac{1}{2\pi\sigma_x\sigma_y\sqrt{1-\varrho^2}} \exp \left\{ -\frac{1}{2(1-\varrho^2)} \left(\frac{x^2}{\sigma_x^2} + \frac{y^2}{\sigma_y^2} - \frac{2xy\varrho}{\sigma_x\sigma_y} \right) \right\}. \quad (6)$$

For this analysis, various functions were evaluated to determine which provided the best fit for the vertex distributions. In the end, the fit is performed using a model that describes the proton density function $\rho(x, y)$ with a main Gaussian component g_M , following the form of Eq. (6), with a large weight w_M , a wide component g_W with a small weight to model wide tails, and a narrow component g_N with a small but negative coefficient $-w_N$ to model a flattened central part:

$$\rho(x, y) = -w_N g_N(x, y) + w_M g_M(x, y) + (1 + w_N - w_M) g_W(x, y). \quad (7)$$

In order to derive a correction for the measured cross section from the VdM scan, the fitted bunch proton densities are used to simulate VdM scans. The product $\Sigma_x \Sigma_y$ from the Monte Carlo simulation of the VdM scan method can then be compared to the value from a direct integration of the nonfactorized bunch proton densities. This yields an estimate of the inaccuracy introduced by using the beam overlap area $\Sigma_x \Sigma_y$, which does not account for the x - y nonfactorization of the bunch proton densities.

However, it is clear that, in contrast to previous years, even the best fit of Eq. (7) shows significant remaining residuals, which results in unreliable estimates of the resulting correction. The reasons for this are not currently understood; possible explanations include that the vertex data used is affected by alignment issues, or that the actual beam shape in fill 6868 includes correlations not similar to those observed previously. As a consequence, we do not currently apply a correction but assess an overall systematic uncertainty of 2.0% to cover the resulting (large) uncertainties observed in the correction.

4.3.2 Offset scan analysis

It is possible to perform a test of x - y nonfactorization of the overlap directly using a pair of offset scans (described in Section 3.2) and the set of VdM scans that took place close to the offset scans. The test is accomplished by making the assumption that the beam geometry did not change during the time these two scan pairs were performed and hence fitting a two-dimensional (2D) model on the VdM and offset data simultaneously gives an accurate shape of the overlap integral.

The fit functions used are built using 2D single Gaussian functions, described by Eq. (6), as well as using 2D higher order super-Gaussian functions:

$$sg(x, y) = \frac{1}{2\pi\sigma_x\sigma_y\sqrt{1-\rho^2}} \exp \left\{ - \left[\frac{1}{2(1-\rho^2)} \left(\frac{x^2}{\sigma_x^2} + \frac{y^2}{\sigma_y^2} - \frac{2xy\rho}{\sigma_x\sigma_y} \right) \right]^p \right\}. \quad (8)$$

Good fit results were found with these two functions as well as various sums of two functions. As the number of free parameters increases in the fit function, the convergence of the fits worsens while the reduced χ^2 values decrease.

To obtain the correction, the volume of the fit function is compared to the volume previously determined from one-dimensional single Gaussian fits performed on the corresponding VdM scans as described in Section 3.1. The corrections obtained with the different fit functions using the first offset scan pair vary between 0.06% and 0.16%, and for the second offset scan pair between 0.14% and 0.27%, with each fit function consistently giving a higher correction for the second pair.

As sources of systematic uncertainties, the variance among different luminometers and the different bunch crossings, the difference between the x and y offset scans, and the uncertainty in the 2D separation due to orbit drift are considered. The uncertainties using the different fit functions vary between 0.05% and 0.17%.

In the two sets of offset scans different correlation parameters and hence different corrections were observed: in the early scan pair (0.1 ± 0.1)% while in the late scan pair (0.2 ± 0.1)%.

This analysis suggests that the correction due to x - y nonfactorization is small compared to the conservative (2%) systematic uncertainty derived from the beam imaging analysis; thus, no correction is applied for this effect in the following.

4.4 Beam-beam effects

Two beam-beam effects are considered in correcting the VdM scan results. The first, beam-beam deflection, accounts for the electrical repulsion of the beams, which increases the lateral separation. It is calculated using the procedure from Ref. [20] and applied as a correction to the beam separation value. The resulting correction is 1.5%, with an uncertainty of 0.2%.

The second is the so-called dynamic- β^* effect, which accounts for the fact that each beam has a defocusing effect on the other. This effect is calculated using reference beam transport simulations [21] that are scaled to the beam energies, the β^* settings, and the measured intensities and convolved beam widths. The resulting correction is -0.5% , with an uncertainty of 0.1%.

Figure 6 shows the final estimates of the beam-beam deflection and dynamic- β^* corrections. Both corrections depend on the value of β^* and the dominant uncertainty in both corrections arises from the uncertainty in the β^* measurement, which is taken to be 15% [22]. Since the corrections are in opposite directions, the resulting uncertainties are thus anticorrelated, resulting

in a correction of 1.0% and a common systematic uncertainty conservatively taken to be 0.2%.

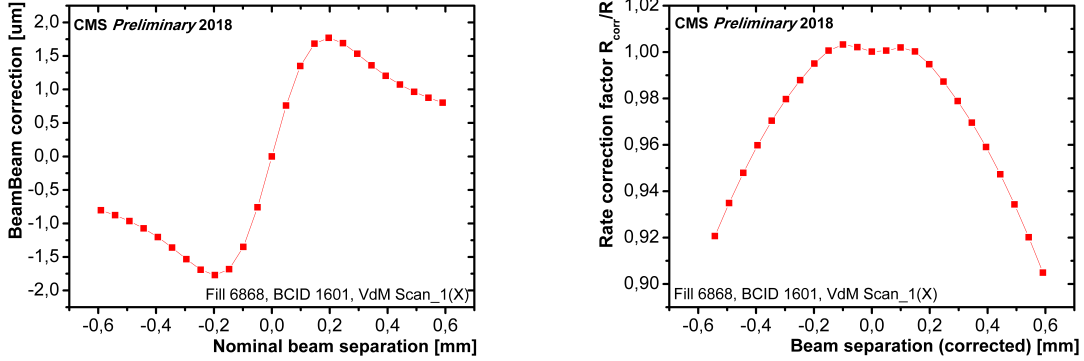


Figure 6: Left: An example of beam-beam deflection estimates as a function of nominal beam separation for BCID 1601. Right: an example of the dynamic- β^* effect on the rate as a function of the beam separation corrected for the beam-beam deflection for BCID 1601.

4.5 Bunch current normalization

Uncertainties in the bunch current used in Eq. (5) arise from two sources. The first arises from the bunch current measurement, which is performed using the FBCTs, which measure the current with a bunch-by-bunch granularity. The DCCT measures the total beam current in each beam; since the absolute scale of this measurement is more precise, the total of the FBCT is normalized to the DCCT measurement. This gives an correction of -0.9% for beam 1 and -1.4% for beam 2 with respect to the FBCT value. The overall uncertainty in the DCCT measurement is 0.2%, which is taken as the first source of uncertainty. (Uncertainty in the relative bunch-by-bunch measurements is not considered.)

The second uncertainty comes from the presence of satellite and ghost charges, where the former refers to charge in the colliding bunch crossing but not in the colliding RF bucket, while the latter refers to charge not in any nominally filled bunch slot. The satellite charges are measured by the FBCT, and the DCCT measurements integrate over all charges, thus include both type of contributions. However, neither actually contributes to the total luminosity, so a correction of the beam intensities is needed in order to obtain an accurate value. For the 2018 VdM fill, these contributions are measured using the LHC longitudinal density monitors [23, 24]. The ghost contribution is 0.13% for beam 1 and 0.16% for beam 2, while the satellites account for 0.04% and 0.05%, respectively. Ghost charge measurement is also performed using the beam-gas imaging method [25] by comparing the beam-gas rates in beam-empty and empty-empty crossings at the LHCb interaction point (IP8), with consistent results of 0.14% for beam 1 and 0.19% for beam 2. Thus, a correction of $+0.4\%$ is applied for the spurious charge contribution from ghosts and satellites. The correction has a 0.1% uncertainty, taking into account the comparison of the LDM and LHCb measurements for the ghost charge and in the absence of an alternative measurement the full correction for the satellite charge.

5 Visible cross section results

Table 1 shows the measured visible cross sections for the different luminometers. The results are shown with all corrections applied. For DT and RAMSES, the visible cross sections are not measured independently because of the lack of bunch-by-bunch data; rather, they are cross-calibrated to the HFOC result.

Note that σ_{vis} is a property of the individual luminometer geometry, acceptance, and efficiency, and thus differs for the different luminometers. It also depends on the measurement algorithm used, hence the difference in the measured σ_{vis} between HFET and HFOC, as well as the large value for PCC, for which many pixel clusters can be detected for a single collision event.

The measured convolved beam width $\Sigma_{x,y}$, on the other hand, is a function of the beam and thus should be measured to be the same by all luminometers. Figure 7 shows the measured Σ_x for HFOC, PLT, BCM1F, HFET, PCC, and vertex counting for the five bunch crossings that have pixel data available; we observe good agreement in the results among all detectors. The two different values of emittance used in this fill are also clearly distinguishable.

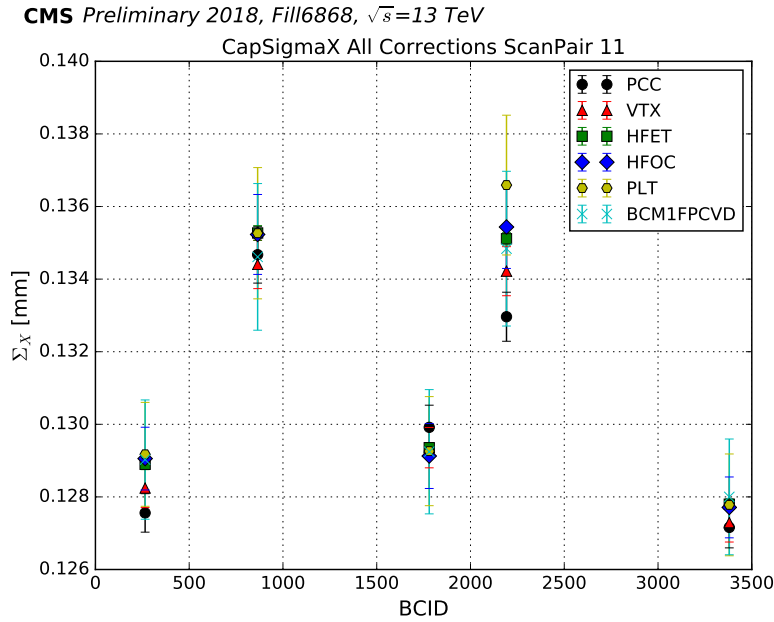


Figure 7: Convolved beam width Σ_x measured in a normal VdM scan for the four online luminometers (HFET, HFOC, PLT, and BCM1F) along with PCC and vertex counting, shown for the five bunch crossings available for PCC and vertices. The measurements from all detectors agree within the statistical uncertainty.

Some variation in the visible cross sections from scan to scan and bunch to bunch is observed. For the scan to scan variation, to cover the possibility of systematic differences between scans, the standard deviation of σ_{vis} for the seven (four normal VdM and three beam imaging) scans is taken; this percentage value is then averaged over the five luminometers used, resulting in an uncertainty of 0.32%. For the bunch to bunch variation, the standard error of the mean after averaging over all bunches is used, resulting in an uncertainty of 0.06%.

After the final calculation of the individual cross sections, we calculate the total integrated luminosity for the periods in the VdM scan fill when no scans were taking place. Since these periods feature a nearly constant luminosity at very low pileup, any effects due to nonlinearity should be negligible, and hence the measurements should be equal among the different luminometers. (Note that only colliding bunches are included in this calculation, so possible noise contributions in the noncolliding bunches do not have any effect.) However, a small difference (approximately 0.5%) is observed. Figure 8 shows the luminosity for the different luminometers during the VdM fill, which shows the overall agreement between the luminometers throughout the fill for a wide range of luminosity; however, the remaining residual differences can be observed in the zoomed region. Table 2 shows the residual differences.

Table 1: Summary of measured visible cross sections for the individual luminometers, where the results have been averaged over all bunches and scans. The “bunch spread” column is determined from the standard deviation of the individual bunch-to-bunch uncertainty, averaged over all scans. The “bunch uncertainty” column shows the overall bunch-to-bunch uncertainty, equal to the spread divided by the square root of the number of bunches.

Luminometer	Measured σ_{vis}	Bunch spread	Bunch uncertainty
BCM1F	210.3 μb	1.3 μb (0.62%)	0.1 μb (0.06%)
HFET	2503.6 μb	13.9 μb (0.56%)	1.3 μb (0.05%)
HFOC	805.9 μb	5.4 μb (0.67%)	0.5 μb (0.06%)
PLT	261.8 μb	1.6 μb (0.61%)	0.1 μb (0.05%)
PCC	5982 mb	37 mb (0.62%)	16.5 mb (0.3%)
VTX	29.12 mb	0.14 mb (0.49%)	0.06 mb (0.2%)

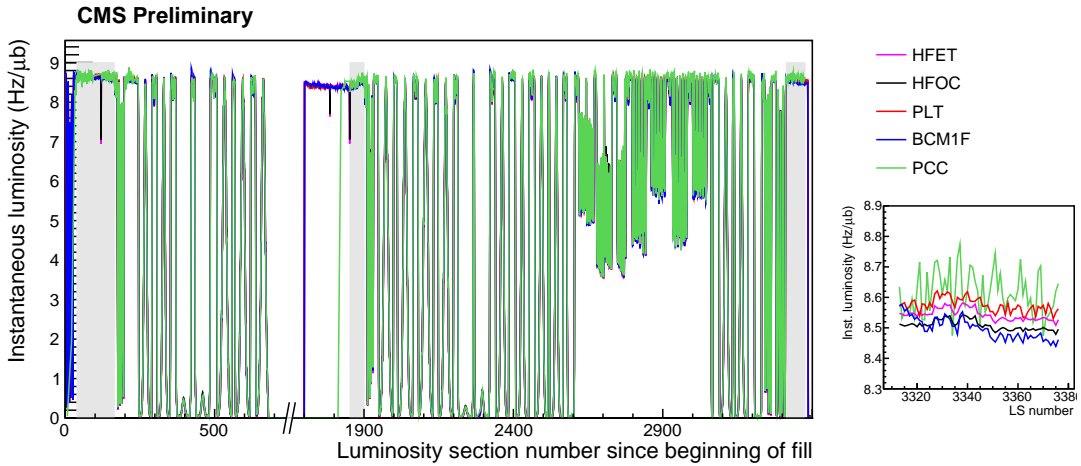


Figure 8: Instantaneous luminosity for the five independent luminometers during the VdM scan fill, showing the general agreement between all five luminometers through all the scans. The period during which CMS was off because of the alarm has been removed. The inset shows a zoom in on one of the periods with stable luminosity, in which the slightly different absolute scales of the different luminometers can be observed. The three gray shaded rectangles indicate the periods used to calculate the total integrated luminosity for the cross-detector comparison.

We assign a systematic uncertainty of 0.5%, the largest variation observed from the average, as a measure of the uncertainty from the cross-detector consistency in the VdM fill.

6 Detector-specific effects

Over the course of the 2018 run, the individual luminosity detectors were affected by several operational issues. In BCM1F and PLT, radiation damage to the sensors caused a loss of efficiency over the course of the year, while HFET and HFOC was similarly affected due to gain loss in the PMTs and fibers in HF. PCC was affected by operational issues resulting in a loss of modules in the PCC measurement.

In 2018, CMS was again able to take advantage of fast luminosity scans with a small beam separation (“emittance scans”) conducted by the LHC to measure these effects. The emittance scans are conducted similarly to a VdM scan, but in normal physics conditions and over a much shorter time. An emittance scan in 2018 consisted of 9 points, with 10 seconds integration time at each scan point, and a maximum beam separation of approximately $4\sigma_b$, so the entire scan

Table 2: Summary of measured integrated luminosity during stable periods in the VdM fill. The third column indicates the difference between the luminosity and the average.

Luminometer	Integrated luminosity (nb^{-1})	Difference from average
BCM1F	41.91	-0.5%
HFET	42.16	+0.1%
HFOC	41.99	-0.3%
PCC	42.31	+0.5%
PLT	42.22	+0.2%

can be conducted in a few minutes. These scans are typically performed at the beginning of the fill and at the end (unless the fill is dumped prematurely). Because of the smaller beam separation and the reduced amount of data at each scan point, the emittance scans do not provide as high a level of precision as the dedicated VdM scans, but they are useful for relative measurements nonetheless.

After the scan, additional offline corrections are applied to emittance scan data. In particular, it was noticed that the bunch current measured by FBCT in the first bunch crossing of the train is approximately 1% too high in comparison to the LHC beam synchrotron radiation telescope (BSRT) [26]. Therefore, currents for all leading bunches in the train were corrected offline; then the FBCT/DCCT correction described in Section 4.5 was performed, and all 2018 emittance scan data were reanalyzed. In addition, it was taken into account that beams are not always exactly at the head-on position in the nonscanning plane in emittance scans, because bunches in the train experience an additional kick from the magnets. This peak position correction results in an increase of approximately 2% in the average visible cross section, but does not reduce bunch to bunch variation or variation between early and late scans.

In the VdM scan fill, the results of the emittance scans taken during the fill agree within uncertainty (typically to better than 0.2%) with those of the dedicated VdM scans, although in normal physics conditions, the emittance scans may be less precise because of nonlinear effects at higher luminosities.

Figure 9 shows an example of how the emittance scan data were used to measure the gain loss affecting the HFOC method. The points show the efficiency of the HFOC luminosity, relative to the efficiency at the time of the VdM scan, as measured using the emittance scan data. A linear fit to the emittance scan data, which is used to derive a resulting correction, is also shown.

Since the emittance scans at the beginning and end of fills are conducted at significantly different SBIL, and because individual bunches within a single fill can also exhibit substantially different SBIL, they can also be used to measure the linearity response of a detector. If a detector shows a slope in the measured cross section as a function of SBIL, nonlinear effects are indicated that can also be measured and corrected using the emittance scan data. The detector-specific nonlinearity corrections derived from the emittance scan data amount to approximately 0.6–2.2%/(Hz/ μb) in PLT, 0.21%/(Hz/ μb) in HFET, and 0.4–1.7%/(Hz/ μb) in BCM1F. The corrections vary depending on the bunch train structure used by the LHC, as the nonlinearity observed is different for leading bunches in a train compared to bunches within a train, and also varies depending on time for PLT and BCM1F because they are affected by the changes in efficiency in those detectors during the 2018 running. For PCC, HFOC, DT, and RAMSES, no additional nonlinearity correction is applied.

Although the measurements from the individual luminometers generally agree well, for the purpose of providing a final luminosity measurement, one luminometer is selected, with other luminometers used to fill gaps when the primary luminometer is unavailable due to oper-

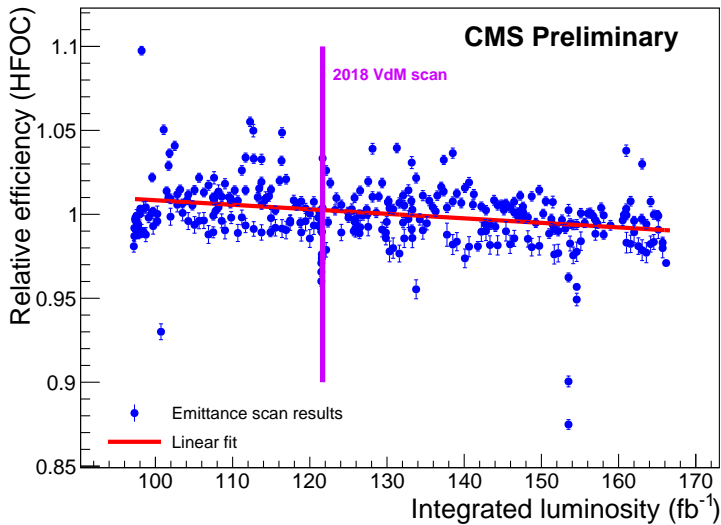


Figure 9: Decrease in HFOC efficiency in 2018 due to aging in the HF. The blue points show the efficiency in the HFOC luminosity measurement, relative to the efficiency at the time of the VdM scan (purple line), as a function of the total integrated luminosity since the beginning of Run 2 in 2015. The red line is a linear fit to the data. Errors shown are statistical.

ational issues. For 2018, the luminosity measurement for a particular time is given by the available luminometer highest among the list HFOC, PCC, PLT, RAMSES, DT, and BCM1F, determined by the best stability and linearity exhibited over the year.

To assess the systematic uncertainty in the HFOC corrections, we look at the residual luminosity in the empty bunches after the corrections are applied; the resulting deviation from zero can be used to estimate the uncertainty. For the type 2 corrections, a systematic uncertainty of 0.4% is assigned based on the variation of the residuals over the course of the year. For the type 1 corrections, the systematic uncertainty calculation is affected by the fact that the residuals show a dependence on SBIL. To avoid double counting of nonlinearity effects, the residuals are instead first corrected using a nonlinearity correction. Once this correction is applied, the remaining variation for HFOC is 0.1%, which is assigned as the systematic uncertainty for the type 1 corrections. Figure 10 shows the residuals for the two correction types (with the nonlinearity correction applied for type 1).

The uncertainties in the PCC corrections are evaluated in a similar fashion and the uncertainty is found to be smaller (0.1% and 0.2% for type 1 and type 2), so the HFOC uncertainty should be sufficient to cover the periods when other methods than HFOC were used in the luminosity determination.

7 Cross-detector comparisons

After corrections for known stability and nonlinearity effects are applied to each detector individually, the luminometer measurements can be compared to each other in order to assess the performance of these corrections.

First, the overall consistency of the individual luminometers with respect to each other is evaluated. This is done by taking the ratio of each luminometer pair. Figure 11 shows the results for several different possible pairs, where periods where the ratio is not well behaved

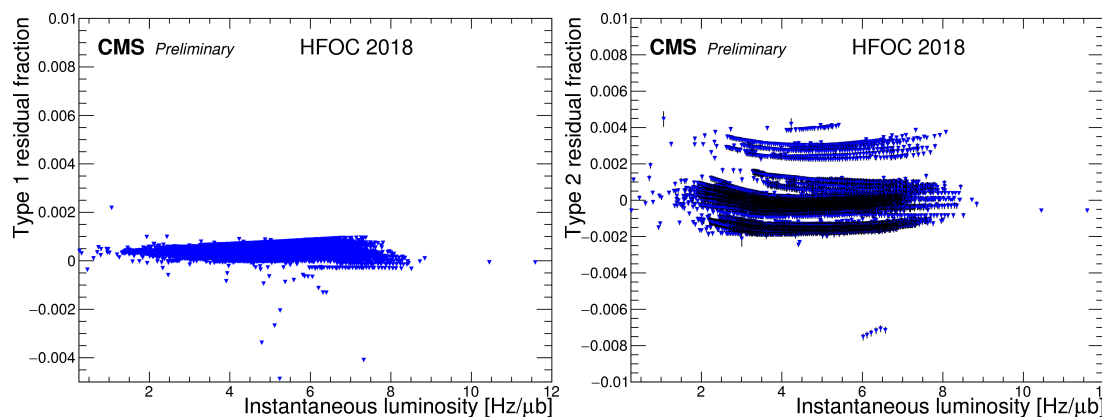


Figure 10: Left: HFOC afterglow correction type 1 residual fractions as a function of instantaneous luminosity. The residual fraction is given by the ratio of the luminosity of the first empty bunch immediately following a colliding bunch to the luminosity of the colliding bunch, after all corrections (including the nonlinearity effect) are applied. Right: Type 2 residual fractions as a function of instantaneous luminosity. These are given by the ratio of the luminosity of the second and following empty bunches after a colliding bunch to the luminosity of the colliding bunch.

due to known detector issues in one detector have been removed. We see that some pairs, such as PCC/HFOC, exhibit excellent stability over the course of the year; in others, such as PLT/HFOC, the overall stability is good although there are still some short periods with unknown issues. The BCM1F ratio plots show that the overall BCM1F scale differs by a few percent from the other luminometers.

To evaluate the uncertainty due to stability, we take the data in Fig. 11 and bin it into a histogram weighted by the luminosity. Some of the resulting distributions are shown in Fig. 12. The standard deviation of each distribution is taken as the relative stability for each pair of luminometers. In the PCC/HFOC, PLT/HFOC, DT/HFOC, and HFET/HFOC cases, we calculate the standard deviation after problematic regions, as observed in Fig. 11, have been excluded.

In addition, the linearity response of the different luminometers is also compared in order to assign a systematic uncertainty in the linearity. This is done in two steps. First, for a given fill, the ratio of the luminosity values given by the two luminometers is plotted as a function of average SBIL. This ratio is then fitted with a line and the slope of the fitted line is taken as the relative nonlinearity for those two luminometers for that fill. Then, the extracted slope is plotted as a function of fill, as for the stability. The results for the 2018 data are shown for different luminometer pairs in Fig. 13. We can see that HFOC, RAMSES, and BCM1F have very small residual nonlinearity with respect to each other, with a slightly larger nonlinearity for PCC/HFOC.

The overall systematic uncertainty due to stability effects is evaluated by looking at the stability plots in the manner of Figs. 11 and 12, but taking the ratio of the best luminometer in the priority list to the second-best luminometer. The results of this test are shown in Fig. 14; we see that there is good agreement and stability overall, although there are a few regions where there are larger differences in the ratio for reasons not currently understood. These are taken into account in the overall systematic uncertainty of 0.6%.

For the linearity correction, we choose the conservative approach of taking the largest mean slope among all the individual detector pairs, which is the PCC/HFOC value of $0.20\%/(\text{Hz}/\mu\text{b})$;

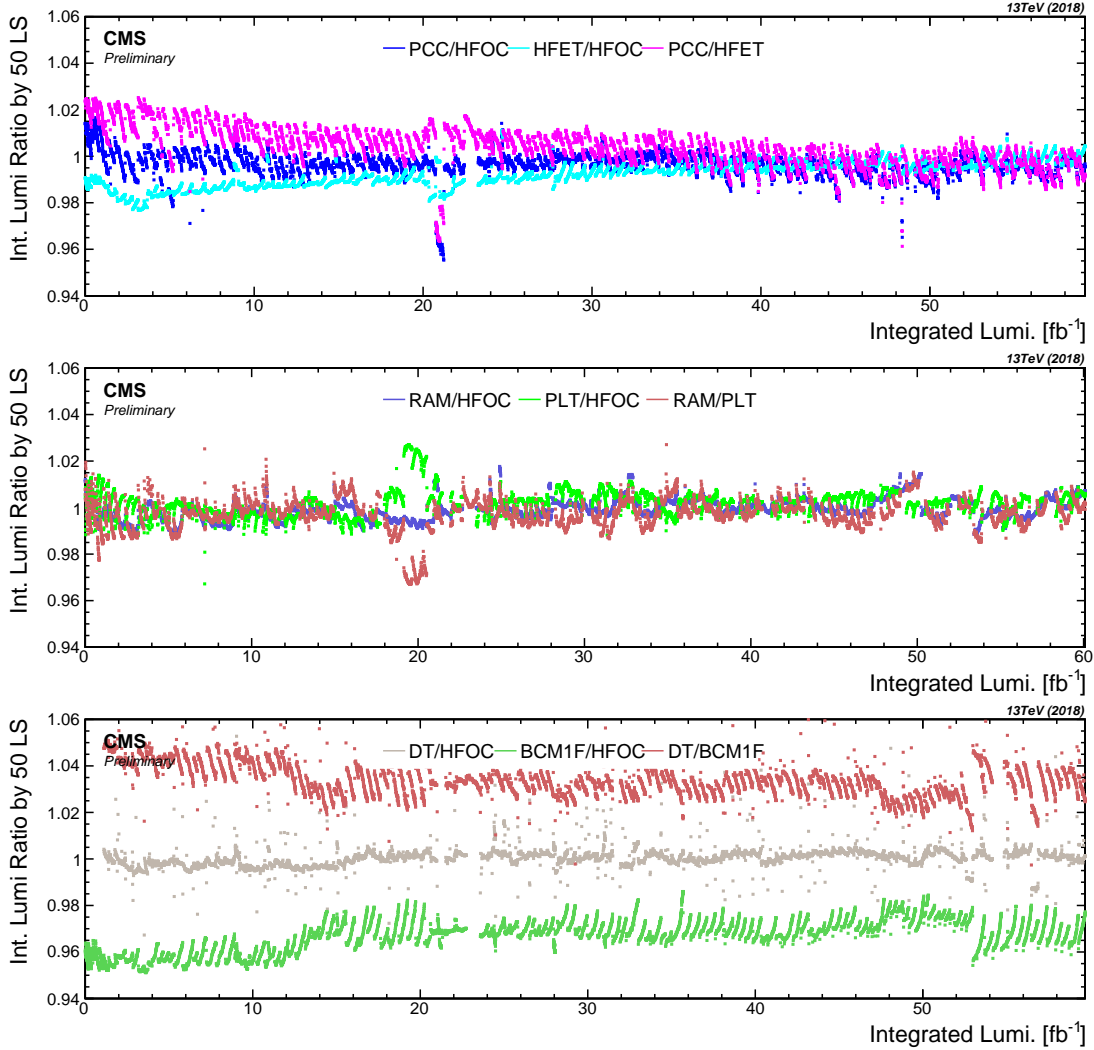


Figure 11: Stability comparisons for different pairs of luminometers across the 2018 data set: (top row) PCC, HFOC, and HFET; (middle row) RAMSES, PLT, and HFOC; (bottom row) DT, BCM1F, and HFOC. Periods where an individual luminometer has known detector issues have been removed.

applied to the overall 2018 luminosity, as the average overall luminosity is approximately $5.5 \text{ Hz}/\mu\text{b}$, this yields a total uncertainty of 1.1% for the linearity. Table 3 summarizes the results of the cross-detector comparisons.

8 Summary

The analysis of the van der Meer (VdM) scans performed by the CMS Collaboration in summer 2018 for the calibration of CMS luminometers to the absolute luminosity scale for proton-proton (pp) collisions at $\sqrt{s} = 13 \text{ TeV}$ has been presented.

Table 4 summarizes the final corrections and systematic uncertainties considered in this analysis. The systematic uncertainties are divided into “normalization” uncertainties; that is, the uncertainties arising from the luminosity calibration in the VdM scan procedure, and “integration” uncertainties, which are the uncertainties arising from the detector operations over the course of the 2018 run.

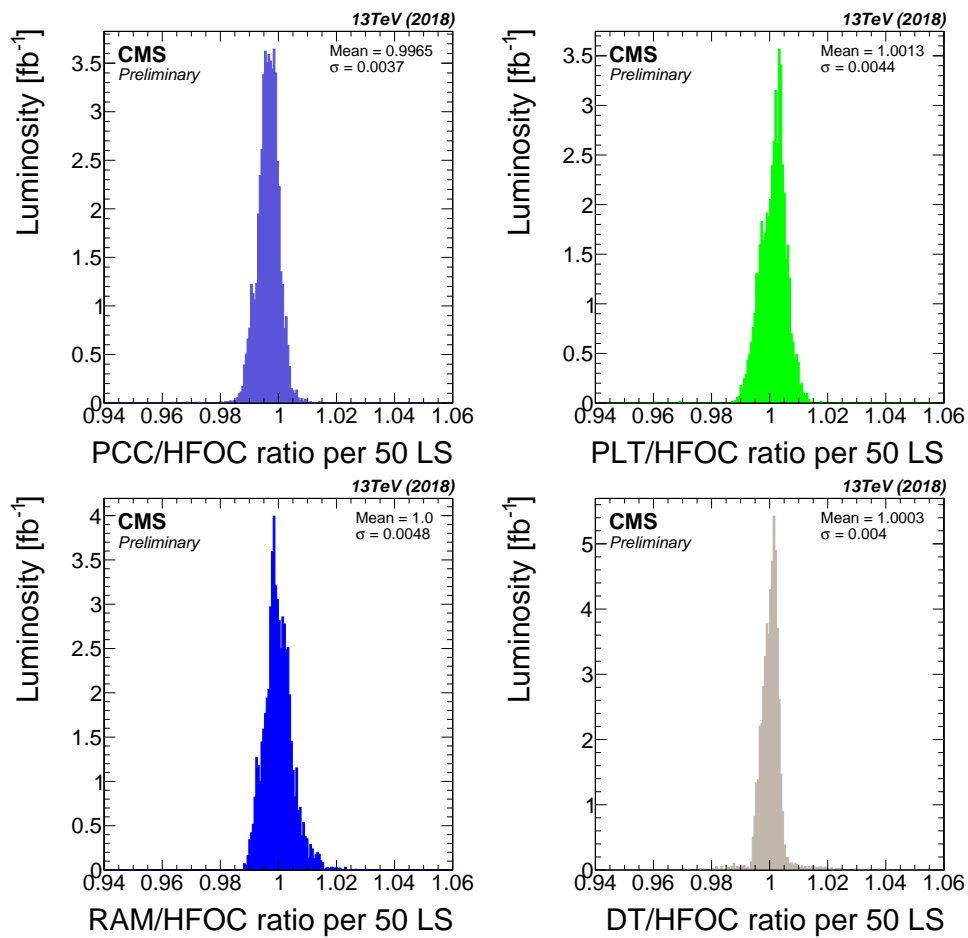


Figure 12: Ratio histograms for different pairs of luminometers: (top left) PCC/HFOC, (top right) PLT/HFOC, (bottom left) RAMSES/HFOC, (bottom right) DT/HFOC. For PCC/HFOC, PLT/HFOC, and DT/HFOC, known problematic regions have been excluded.

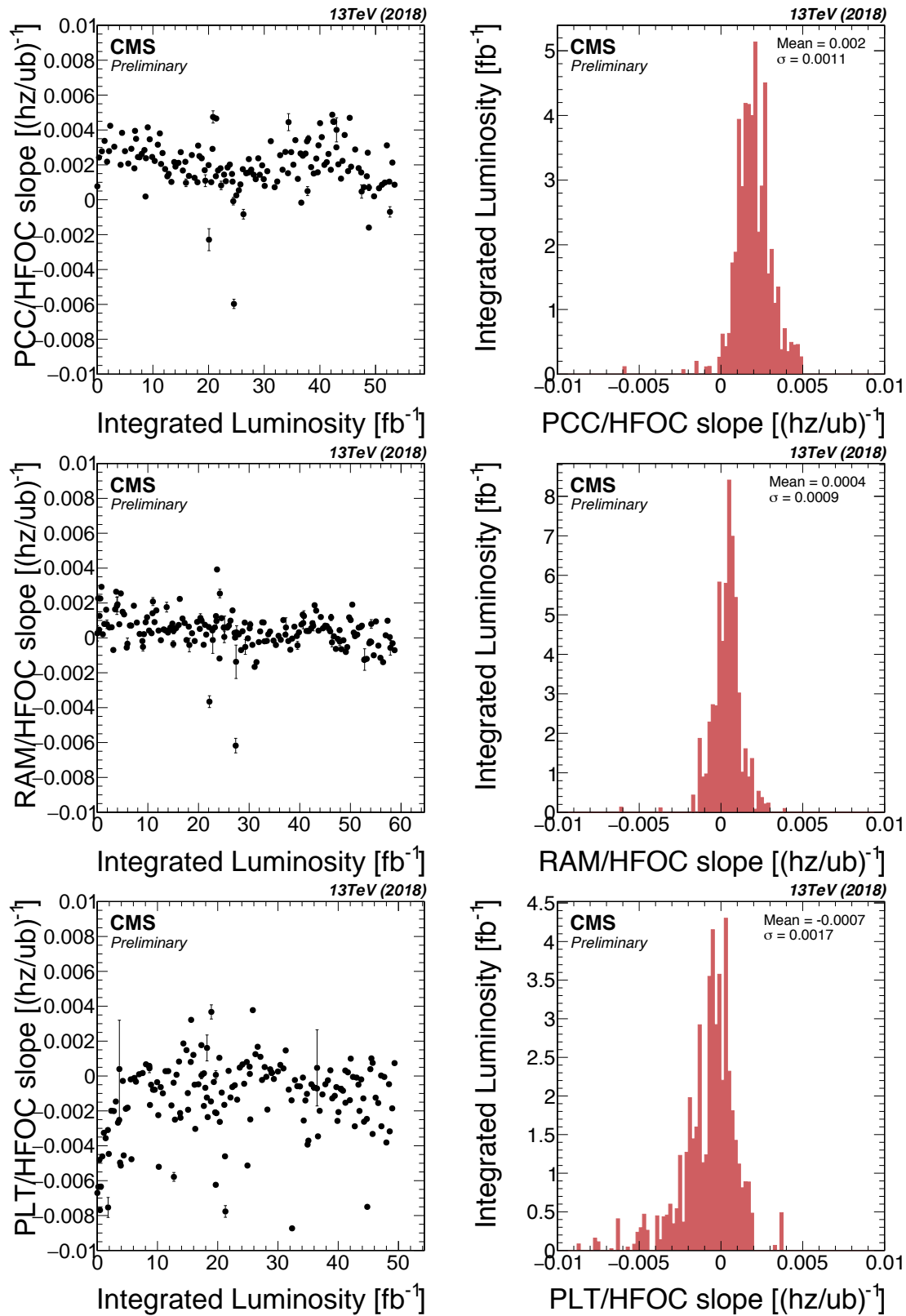


Figure 13: Results of the linearity studies for all 2018 fills for three different detector pairs: (top row) PCC/HFOC, (middle row) RAMSES/HFOC, (bottom row) PLT/HFOC. The left column of plots shows the slopes of linear fits per fill as a function of integrated luminosity over the course of 2018. The right plot shows the same slopes but binned and weighted according to the luminosity in that fill.

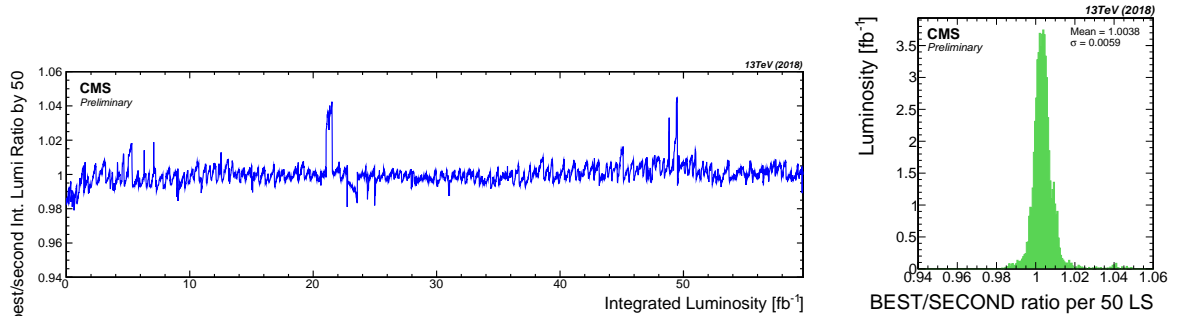


Figure 14: Stability tests done between the best and second-best luminometer in the priority list. Left: Ratio as a function of time. Right: Histogram of ratio values, weighted by luminosity. The standard deviation of the histogram is taken as the resulting systematic uncertainty.

Table 3: Summary of cross-detector comparisons. For each pair of detectors compared, each of the following is considered: the mean of the ratio between the two luminosity measurements, the standard deviation (SD) of the per-fill luminosity ratios, the mean of the slopes between the two measurements, and the standard deviation of the per-fill slopes. For PCC/HFOC, PLT/HFOC, DT/HFOC, and HFET/HFOC, problematic regions are excluded, as described in the text.

Luminometer pair	Mean ratio	SD ratio (%)	Mean slope (%/(Hz/ μ b))	SD slope (%/(Hz/ μ b))
PCC/HFOC	0.997	0.37	0.20	0.11
PLT/HFOC	1.001	0.44	-0.07	0.17
RAMSES/HFOC	1.000	0.48	0.04	0.09
DT/HFOC	1.000	0.40	0.01	0.07
BCM1F/HFOC	0.967	0.65	-0.20	0.15
HFET/HFOC	0.992	0.52	-0.09	0.07

The dominant uncertainty contributing to the luminosity scale calibration, as described in Sections 4 and 5, is from the x - y nonfactorization of the colliding proton bunch densities. All normalization uncertainties are treated as uncorrelated, giving a total of 2.1% in the luminosity scale calibration.

The integration uncertainty of 1.3% includes the detector-specific uncertainties discussed in Section 6 and the cross-detector stability and linearity uncertainties covered in Section 7. In addition, the uncertainty in the integrated luminosity due to the deadtime of the CMS DAQ system is smaller than 0.1%.

The integration and normalization uncertainties are treated as uncorrelated. In summary, the total uncertainty in the luminosity measurement in 2018 is 2.5% for CMS data recorded in pp collisions at $\sqrt{s} = 13$ TeV.

References

- [1] CMS Collaboration, “The CMS experiment at the CERN LHC”, *JINST* **3** (2008) S08004, doi:10.1088/1748-0221/3/08/S08004.
- [2] P. Lujan, “Performance of the Pixel Luminosity Telescope for luminosity measurement at CMS during Run 2”, *PoS* **314** (2017) 504, doi:10.22323/1.314.0504.

Table 4: Summary of the systematic uncertainties entering the CMS luminosity measurement for $\sqrt{s} = 13$ TeV pp collisions collected in 2018. When applicable, the percentage correction is shown.

	Systematic	Correction (%)	Uncertainty (%)
Normalization	Length scale	-0.8	0.2
	Orbit drift	0.2	0.1
	x - y nonfactorization	0.0	2.0
	Beam-beam deflection	1.5	0.2
	Dynamic- β^*	-0.5	
	Beam current calibration	2.3	0.2
	Ghosts and satellites	0.4	0.1
	Scan to scan variation	—	0.3
	Bunch to bunch variation	—	0.1
	Cross-detector consistency	—	0.5
	Background subtraction	0 to 0.8	0.1
Integration	Afterglow (HFOC)	0 to 4	$0.1 \oplus 0.4$
	Cross-detector stability	—	0.6
	Linearity	—	1.1
	CMS downtime	—	<0.1
	Total		2.5

- [3] M. Hempel, “Development of a novel diamond based detector for machine induced background and luminosity measurements”. PhD thesis, DESY, Hamburg, 2017. doi:10.3204/PUBDB-2017-06875.
- [4] CMS Collaboration, “The CMS trigger system”, *JINST* **12** (2017) P01020, doi:10.1088/1748-0221/12/01/P01020, arXiv:1609.02366.
- [5] S. van der Meer, “Calibration of the effective beam height in the ISR”, Technical Report CERN-ISR-PO-68-31, 1968.
- [6] CMS Collaboration, “CMS luminosity based on pixel cluster counting - Summer 2013 update”, CMS Physics Analysis Summary CMS-PAS-LUM-13-001, 2013.
- [7] CMS Collaboration, “CMS luminosity measurement for the 2016 data taking period”, CMS Physics Analysis Summary CMS-PAS-LUM-17-001, 2017.
- [8] CMS Collaboration, “CMS luminosity measurement using 2016 proton-nucleus collisions at $\sqrt{s_{NN}} = 8$ TeV”, CMS Physics Analysis Summary CMS-PAS-LUM-17-002, 2018.
- [9] CMS Collaboration, “CMS luminosity measurement for the 2017 data-taking period at $\sqrt{s} = 13$ TeV”, CMS Physics Analysis Summary CMS-PAS-LUM-17-004, 2018.
- [10] ATLAS Collaboration, “Luminosity determination in pp collisions at $\sqrt{s} = 8$ TeV using the ATLAS detector at the LHC”, *Eur. Phys. J. C* **76** (2016) 653, doi:10.1140/epjc/s10052-016-4466-1, arXiv:1608.03953.
- [11] ALICE Collaboration, “Measurement of visible cross sections in proton-lead collisions at $\sqrt{s_{NN}} = 5.02$ TeV in van der Meer scans with the ALICE detector”, *JINST* **9** (2014) P11003, doi:10.1088/1748-0221/9/11/P11003, arXiv:1405.1849.
- [12] LHCb Collaboration, “Precision luminosity measurements at LHCb”, *JINST* **9** (2014) P12005, doi:10.1088/1748-0221/9/12/P12005, arXiv:1410.0149.

- [13] CMS Collaboration, “Description and performance of track and primary-vertex reconstruction with the CMS tracker”, *JINST* **9** (2014) P10009, doi:10.1088/1748-0221/9/10/P10009, arXiv:1405.6569.
- [14] CMS Collaboration, “CMS luminosity measurement for the 2015 data taking period”, CMS Physics Analysis Summary CMS-PAS-LUM-15-001, 2016.
- [15] C. Barschel et al., “Results of the LHC DCCT calibration studies”, Technical Report CERN-ATS-Note-2012-026 PERF, 2012.
- [16] D. Belohrad et al., “The LHC fast BCT system: A comparison of design parameters with initial performance”, Technical Report CERN-BE-2010-010, 2010.
- [17] M. Gasior, J. Olexa, and R. Steinhagen, “BPM electronics based on compensated diode detectors — results from development systems”, *Conf. Proc. C* **1204151** (2012) 44.
- [18] M. Zanetti, “Beams scan based absolute normalization of the CMS luminosity measurement”, Technical Report CERN-Proceedings-2011-001, 2011.
- [19] M. Klute, C. Medlock, and J. Salfeld-Nebgen, “Beam imaging and luminosity calibration”, *JINST* **12** (2017) P03018, doi:10.1088/1748-0221/12/03/P03018, arXiv:1603.03566.
- [20] W. Kozanecki, T. Pieloni, and J. Wenninger, “Observation of beam-beam deflections with LHC orbit data”, Technical Report CERN-ACC-NOTE-2013-0006, 2013.
- [21] A. Babaev, “Beam-dynamic effects at the CMS BRIL van der Meer scans”, *JINST* **13** (2018) C03028, doi:10.1088/1748-0221/13/03/C03028.
- [22] R. Alemany-Fernández et al., “Cross-calibration of the LHC transverse beam-profile monitors”, in *Proceedings, 8th International Particle Accelerator Conference (IPAC 2017): Copenhagen, Denmark, May 14-19, 2017*, p. MOPAB130. 2017. doi:10.18429/JACoW-IPAC2017-MOPAB130.
- [23] A. Jeff et al., “Longitudinal density monitor for the LHC”, *Phys. Rev. ST Accel. Beams* **15** (2012) 032803, doi:10.1103/PhysRevSTAB.15.032803.
- [24] A. Jeff, “A longitudinal density monitor for the LHC”. PhD thesis, Liverpool University, 2012.
- [25] C. Barschel, “Precision luminosity measurement at LHCb with beam-gas imaging”. PhD thesis, RWTH Aachen University, 2014.
- [26] A. S. Fisher, “Expected performance of the LHC synchrotron-light telescope (BSRT) and abort-gap monitor (BSRA)”, LHC Performance Note 014, 2010.

A Additional figures

CMS Preliminary 2018, Fill 6868, $\sqrt{s}=13$ TeV

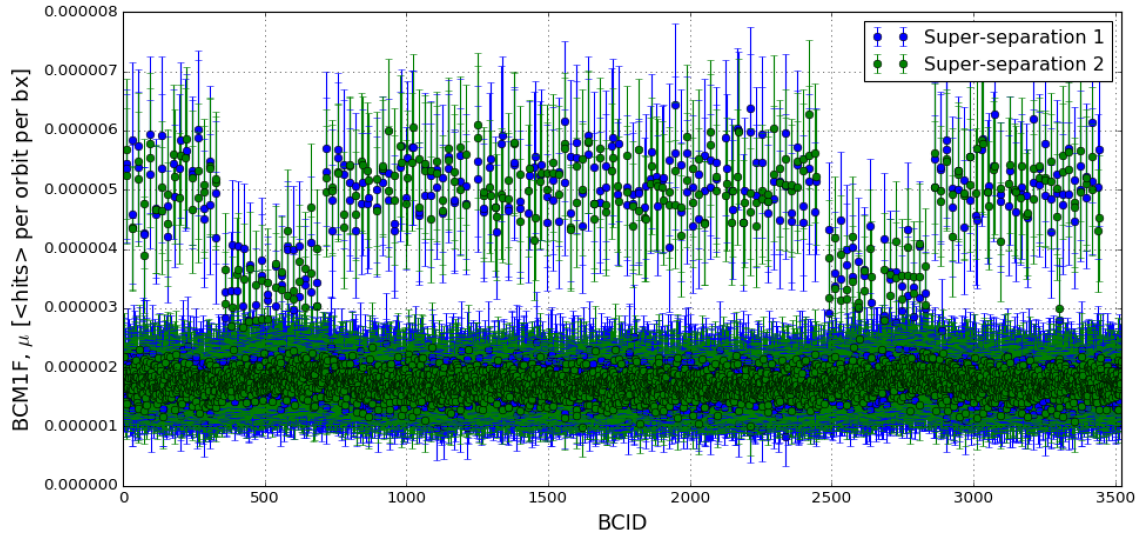


Figure 15: Background measured in the two “super separation” periods by the BCM1F detector. The top band corresponds to colliding bunches, which have beam-induced background from both beams. The middle band contains bunches which are filled in one beam but not the other, so there is only a beam-induced contribution from one beam. The bottom band contains bunches which are not filled in either beam, so this corresponds to the detector noise.

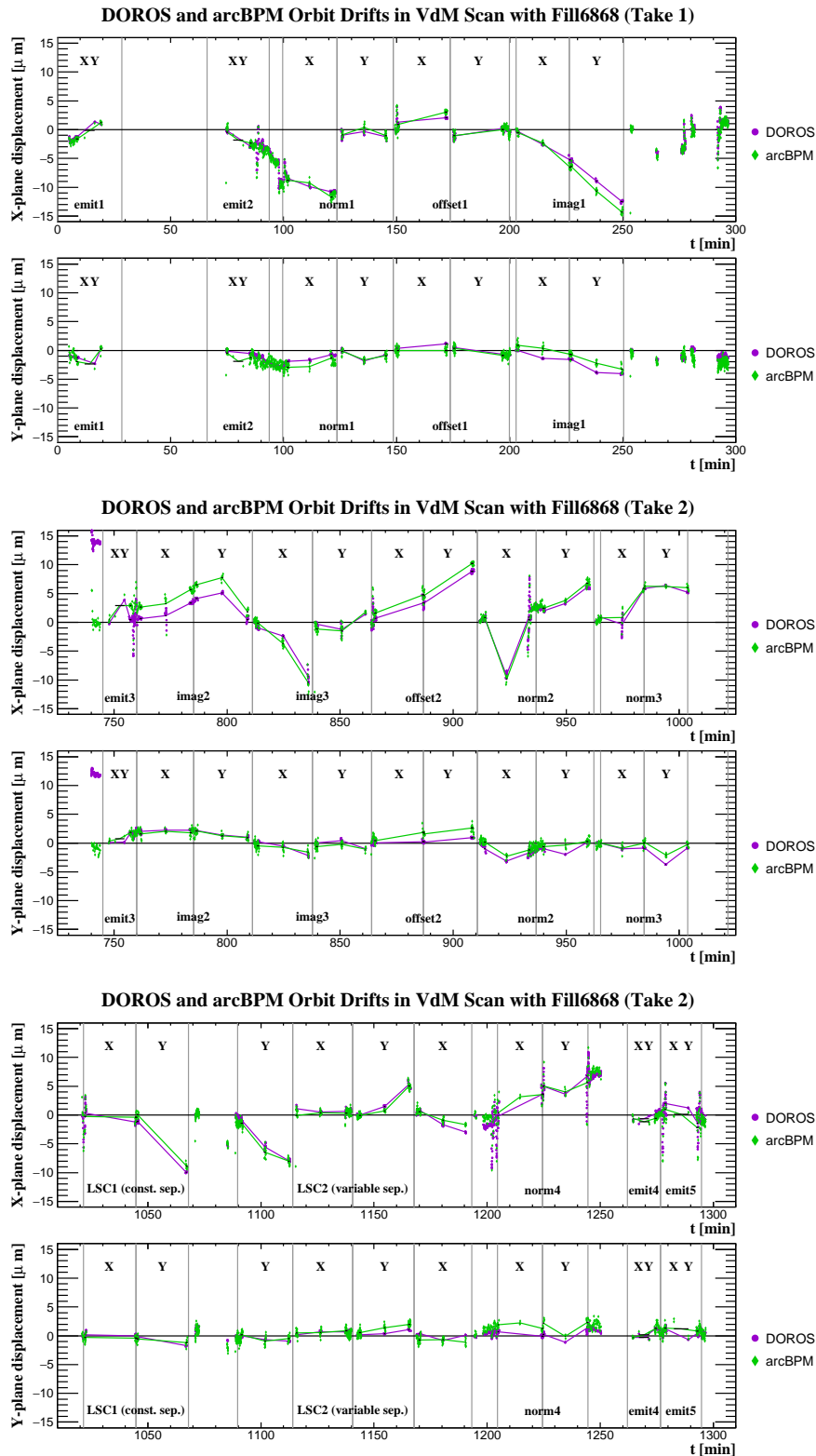


Figure 16: Results of the orbit drift measurement. The top pair of plots covers the time range before the alarm at CMS, the middle pair covers the first part of the time after the alarm, and the bottom pair covers the last part of the scan. In each pair the x drift is shown in the top panel and the y in the bottom panel. The dots represent the beam position measured at the times when the beams are head-on before, during, and after each scan, as given by the DOROS and arc BPMs in μm . The lines are the fits used to provide the orbit drift correction for each step of the scan.

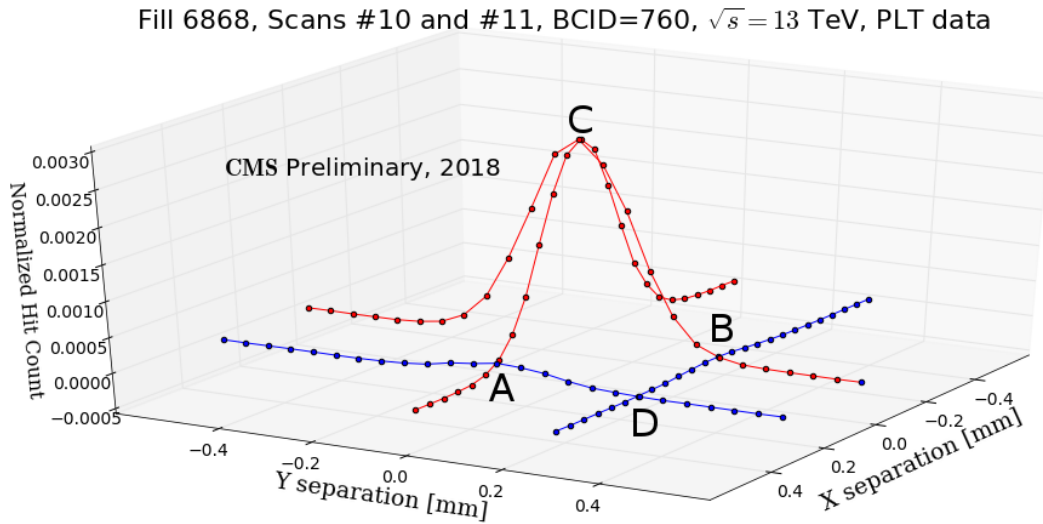


Figure 17: The beam separation vs. rate (normalized by beam currents) for BCID 760 from the PLT data. The red and the blue lines represent the regular VdM and the offset scans, respectively. At the points A, B, C, and D, the same point is sampled in two different scans. This makes compatibility checks possible.

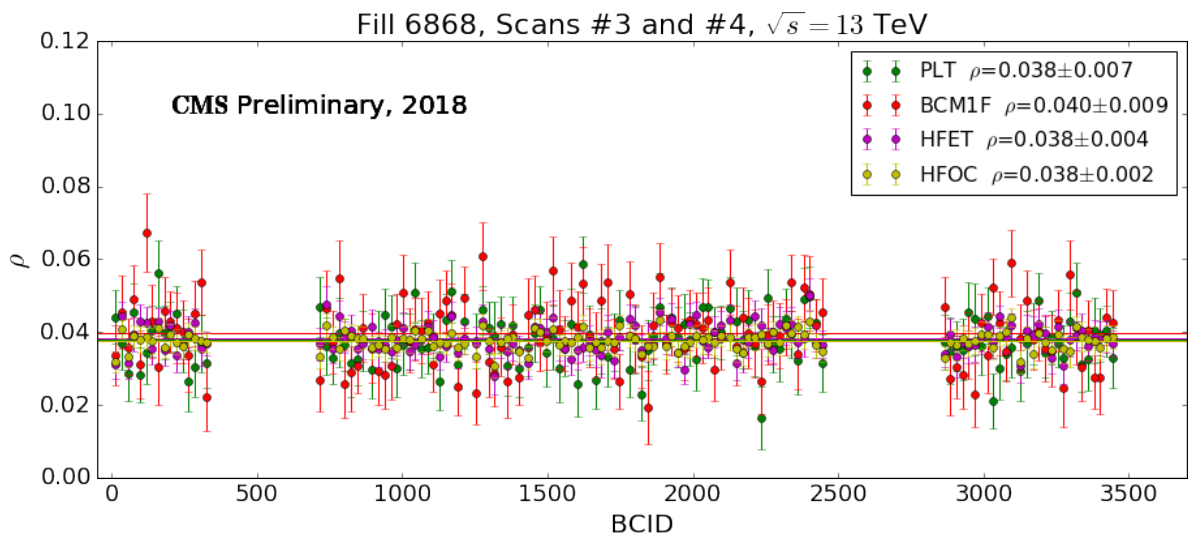


Figure 18: The ρ correlation parameter obtained from the offset scan analysis for each BCID for PLT, BCM1F, HFET, and HFOC.

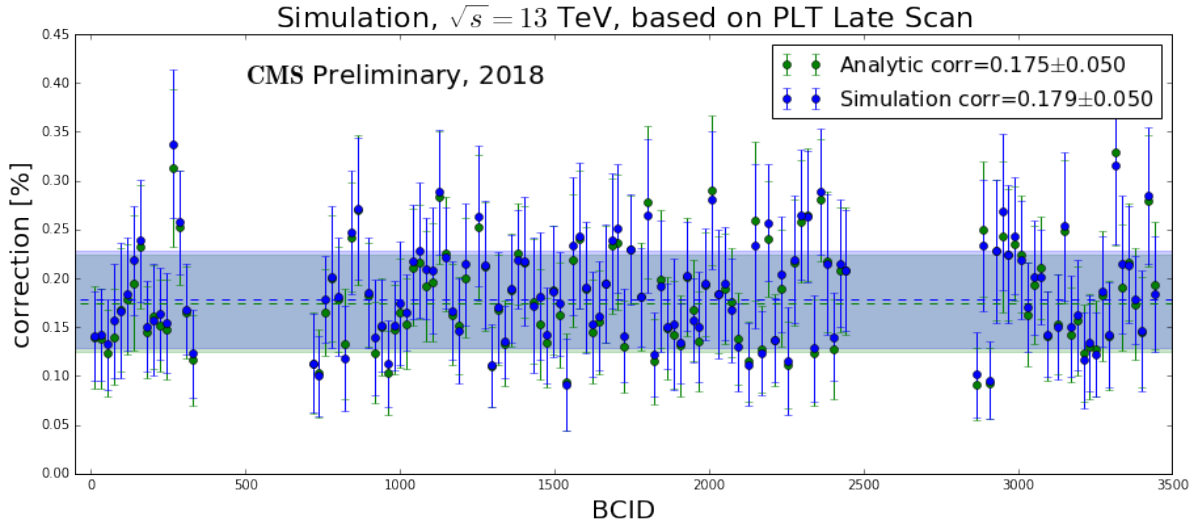


Figure 19: The corrections using the offset scan analysis obtained from analytic calculation and simulation are compared to validate the simulation method. The plot shows this comparison for single Gaussian shapes fitted on the PLT data in the late scan. The dashed lines and colored bands indicate the overall average and its uncertainty, respectively, for the two methods.

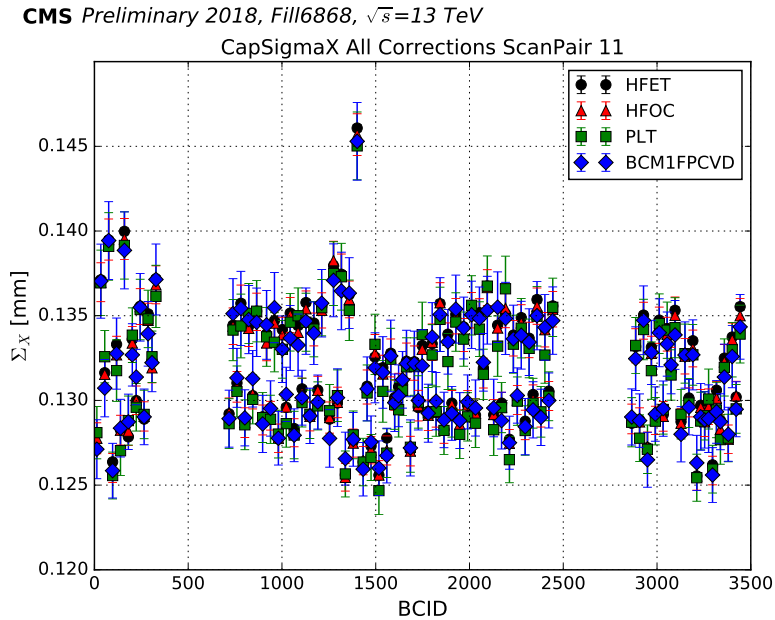


Figure 20: Convolved beam width (Σ_x) measured in a normal VdM scan for all colliding bunches for all online luminometers (HFET, HFOC, PLT, BCM1F pCVD). The measurements from all detectors agree within the statistical uncertainty.

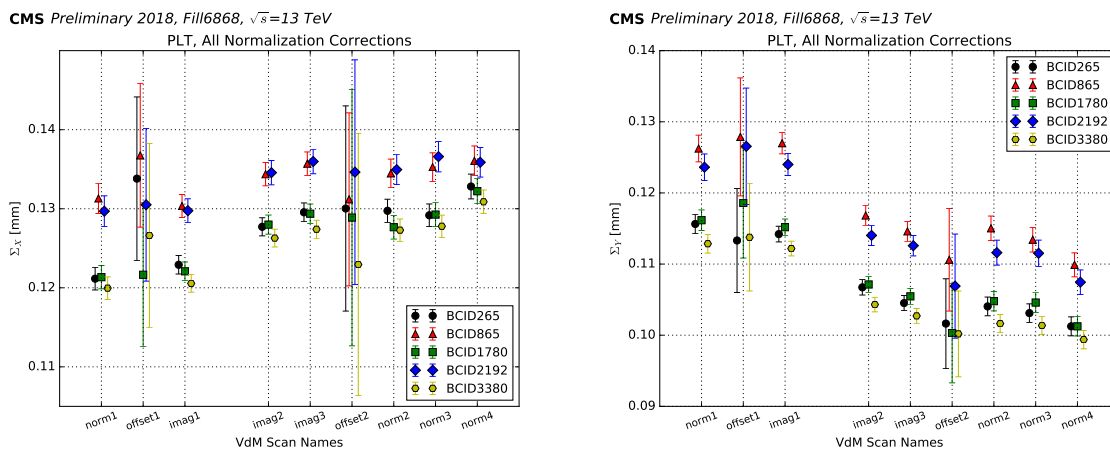


Figure 21: Convolved beam width measured by PLT in the x (left) and y (right) dimension (Σ_x and Σ_y) after all normalization corrections have applied for the five bunch crossings with PCC data available. The uncertainty shown is statistical. The beam size increases in the x direction and decreases in y over time.

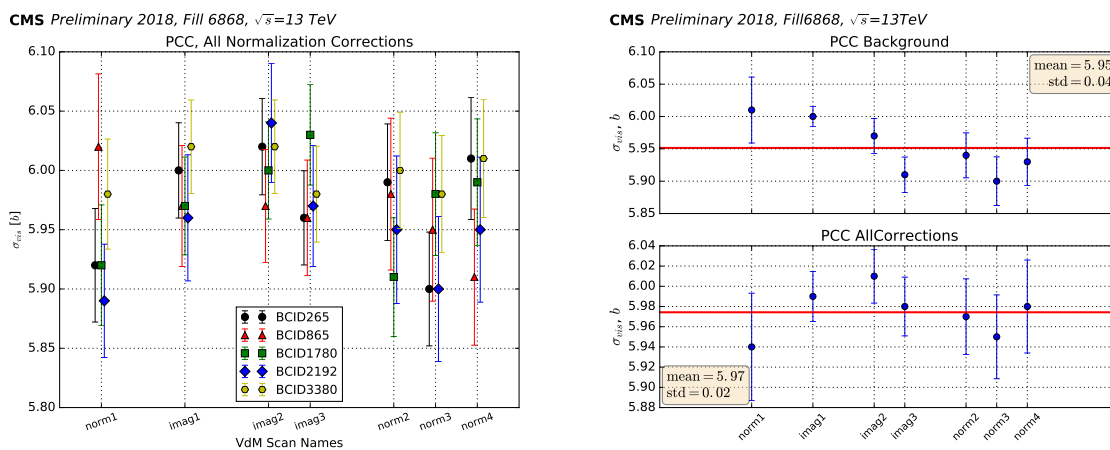


Figure 22: Left: Measured PCC visible cross section for all VdM scans, for the five bunch crossings with pixel data available. The uncertainty shown is statistical. Right: The measured visible cross section for each scan, together with the weighted average (red line), with only the background correction applied (top) and with all corrections applied (bottom).

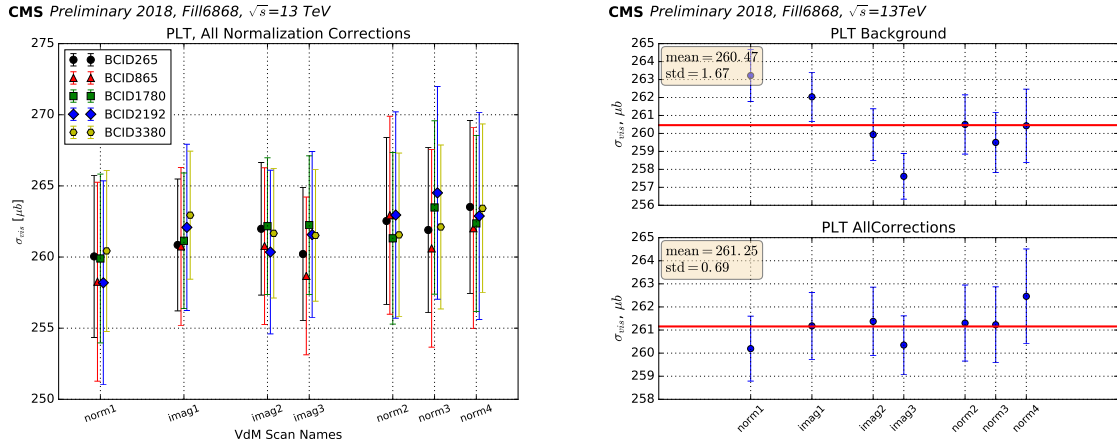


Figure 23: Left: Measured PLT visible cross section for all VdM scans, for the five bunch crossings with pixel data available. The uncertainty shown is statistical. Right: The measured visible cross section for each scan, together with the weighted average (red line), with only the background correction applied (top) and with all corrections applied (bottom).

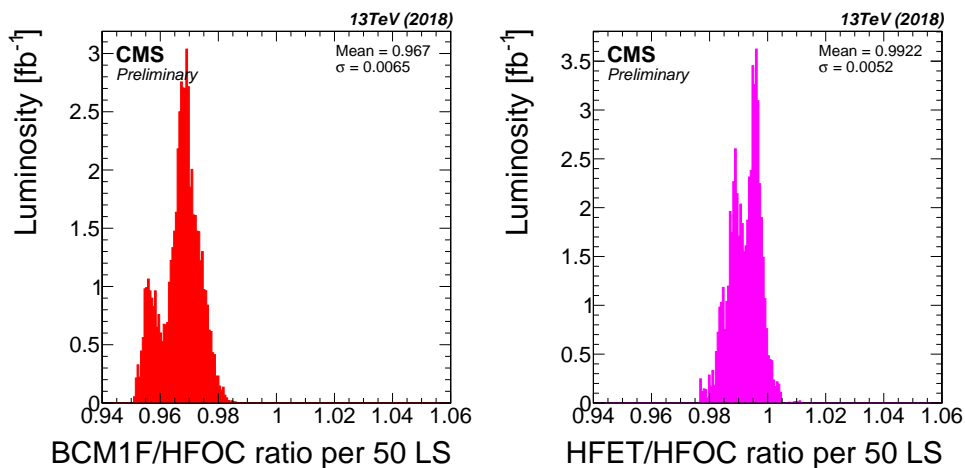


Figure 24: Ratio histograms for different pairs of luminometers: (left) BCM1F/HFOC, (right) HFET/HFOC. For HFET/HFOC, known problematic regions have been excluded.

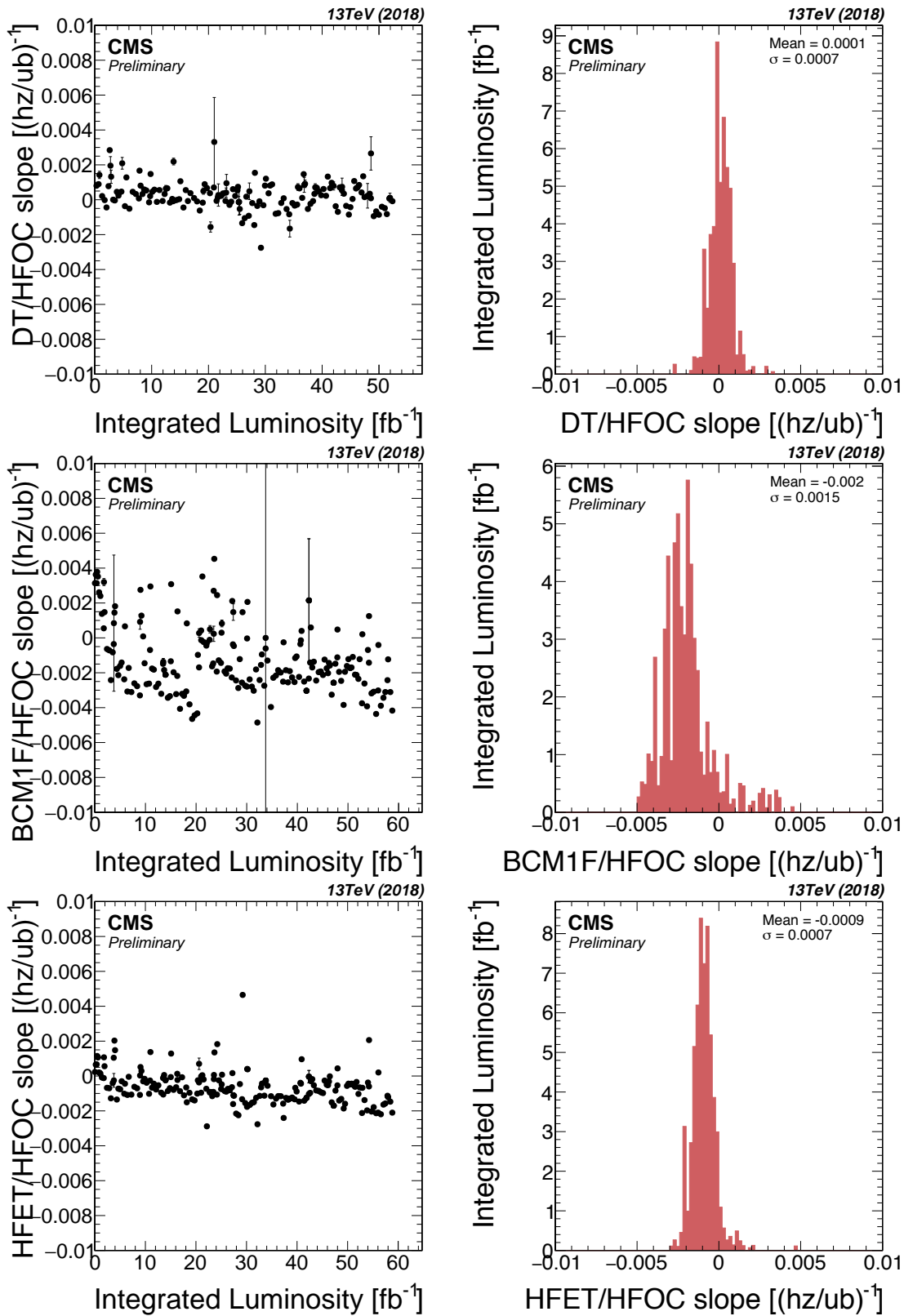


Figure 25: Results of the linearity studies for all 2018 fills for three different detector pairs: (top row) DT/HFOC, (middle row) BCM1F/HFOC, (bottom row) HFET/HFOC. The left column of plots shows the slopes of linear fits per fill as a function of integrated luminosity over the course of 2018. The right plot shows the same slopes but binned and weighted according to the luminosity in that fill.